Characterization of subduction zone serpentinites using attenuated total reflection infrared (ATR-IR)

spectroscopy: Case studies from the Sanbagawa metamorphic belt in southwest Japan and the Yuli metamorphic

belt in eastern Taiwan

（沈み込み帯における蛇紋石の減衰全反射赤外分光法による特性の評価研究：西南日本三波川変成帯

及び東台湾玉里変成帯に産する蛇紋岩体の例）

SAKAGUCHI Ilona Talvikki

（坂口 イロナ タルビッキ）

A dissertation for the degree of Doctor of Science

Department of Earth and Environmental Sciences,

Graduate School of Environmental Studies, Nagoya University

（名古屋大学大学院環境学研究科地球環境科学専攻学位論文 博士（理学））

2021

CONTENTS

OVERVIEW

Serpentinites are metamorphic rocks, which are formed when ultramafic rocks are hydrated. Serpentinites are mostly comprised of serpentine minerals, which contain ~13 wt% of molecularly bound water, and they are one of the most important water-bearing minerals in the subduction zone. Fluids released by serpentinite dehydration reactions play a key role in many subduction zone processes, such as in elemental cycling, subduction zone melt formation and in triggering earthquakes at intermediate depths (~50-300 km) in the subduction zone. Recently, many researchers have become interested in studying the microstructures and composition of subduction zone serpentinites in order to understand the dehydration processes of serpentinites in more detail and to build a more comprehensive model of subduction zone hydrodynamics. The challenge with studying subduction zone serpentinites is that they are often almost monomineralic, being composed mainly of serpentine minerals, making detailed petrological interpretations about their metamorphic history difficult. Hence, to get a better understanding of serpentinization processes, it is necessary to look at variations within the crystal structure of serpentine minerals.

One useful method that can be used to study variations in the crystal structure of serpentinite minerals is attenuated total reflection infrared spectroscopy, abbreviated as ATR-IR. The ATR-IR method is an improvement on the more commonly used transmission infrared spectroscopy method since, unlike in the transmission infrared spectroscopy method, the ATR-IR method allows measurements to be made from regular one-sided petrographic thin sections, which both cuts down of sample preparation time and preserves the microstructures in the sample. The ATR-IR method is based on measuring the vibration of molecular bonds in the crystal structure of minerals by running an infrared beam through an internal reflection element on to the sample and then directly back to the spectrometer, which allows measurements to be

made from the surface of the sample. This method makes it possible to look at slight differences in the crystal structure of serpentine minerals by observing the variation in the intensity and wavenumber values of serpentine mineral infrared absorbance spectra. The absorbance of the O-H bond is especially strong in the mid-infrared region measured for this study, which is why infrared spectroscopy has often been used to study the behavior of hydroxyl groups in rock and mineral samples.

In this PhD thesis, I studied the microstructure and composition of subduction zone serpentinites from two high pressure metamorphic belts in East Asia, the Sanbagawa metamorphic belt in southwest Japan and the Yuli metamorphic belt in eastern Taiwan, using ATR-IR spectroscopy and electron microprobe analysis (EPMA) to see if the ATR-IR method could be used to differentiate between different types of serpentine minerals and if the composition and microstructures in the high temperature serpentine mineral variety, antigorite, could be linked to metasomatic events in the subduction zone. In addition, a new data-processing algorithm was developed to study ATR-IR mapping data of serpentinites. The algorithm that was developed can be also applied to study various other types of vibrational spectroscopy data and the details on how to apply this new method to quantitatively process large amounts of spectral mapping data are outlined in the last chapter of the thesis.

Part 1.

Antigorite, chrysotile and lizardite are the three main serpentine mineral varieties. The three serpentine minerals are stable in different metamorphic conditions and thus identifying them is of great importance when studying the metamorphic history of serpentinites. However, distinguishing antigorite, chrysotile and lizardite from a petrological thin section can be challenging because of their similar optical properties and chemical composition. In this study, I studied the ATR-IR spectra of antigorite, chrysotile and lizardite from serpentinites from the

Shiraga area in the Sanbagawa metamorphic belt, and found out that each serpentine mineral had a distinct ATR-IR spectra, which could be used to distinguish the three minerals from each other. There was an especially large difference in the Si-O absorbance bands of the three serpentine minerals and the wavenumber value of the Si-O absorbance band could be used to construct phase maps showing the textural relationships between antigorite, chrysotile and lizardite. Furthermore, an ATR-IR map of antigorite veins running through an antigorite matrix in combination with EPMA measurements, revealed that the wavenumber values of antigorite O-H absorbance bands are strongly dependent on the Fe content of antigorite.

Part 2.

Antigorite is a high temperature serpentine mineral variety and it is the most common type of serpentine mineral in the subduction zone. The dehydration of antigorite releases significant amounts of water-rich fluids into the subduction channel and thus compositional variation and variation in the crystal structure of antigorites in subduction zone serpentinites is of special interest to many researchers. In this study, I used ATR-IR spectroscopy and electron microprobe measurements (EPMA) to study the crystal structure and chemical composition of antigorite serpentinites collected from the high pressure metamorphic Yuli belt in eastern Taiwan. The samples were collected from serpentinite bodies in the Wanjung, Juisui and Chinshuichi regions of the Yuli belt. Seven samples from the three serpentinite bodies were chosen for more detailed analyses based on their mineral assemblage and a variety of microstructures, such as areas with metamorphic olivine and samples with different types of veins that could be linked to possible subduction zone fluid flow events. In this study, I focused on looking at the variation in the highest intensity Si-O and O-H absorbance peaks of the measured antigorites. The overall results of ATR-IR measurements are somewhat scattered but a few interesting trends could be recognized. The main observation was again that the Fe

content of antigorite had a significant effect on the wavenumber value of antigorite O-H absorbance bands. Indeed, there was significant variation in the Fe content of the measured samples, which might indicate iron mobilization in the subduction zone. Also the Al and Si content of the samples varied, with measurements made from antigorite veins in talc rich samples being more Si-rich, indicating the inflow of fluids with high silica activity. Furthermore, field observations of rogingite and magnesite veins and well as chlorite, epidote, albite and amphibole rich contact zone between the serpentinites and the surrounding metasediments show that the Yuli belt serpentinites were affected by active subduction zone metasomatism.

Part 3.

In the past 20 years, many advances have been made in the field of vibrational spectroscopy, which includes the methods of Raman spectroscopy and infrared spectroscopy. The methods, which were once used mainly for simple mineral identification, are now being applied more frequently to conduct more advanced mineralogical research, such as geothermobarometry. A new data-processing algorithm that was developed to study the absorbance intensities and wavenumber values of ATR-IR spectra of serpentinites, could be also applied to study other types of spectral data. This chapter gives a detailed outline of the different functions of this data-processing algorithm as well as suggests several different applications of mineral spectroscopy that could benefit from using this method. Also, this final chapter discusses our plans of further developing this algorithm to include more complex filtering and fitting functions as well as developing more advanced options for spectral calculations.

Part 1:

Attenuated total reflection infrared (ATR-IR) spectroscopy of antigorite, chrysotile and

lizardite from the Shiraga area serpentinites in the Sanbagawa metamorphic belt,

southwest Japan

ABSTRACT

Attenuated total reflection infrared (ATR-IR) spectroscopy allows measurements to be made directly from the surface of one-sided, diamond polished thin sections of geological samples. This method reduces the sample preparation time significantly when compared to other IR spectroscopy methods. This opens the possibility of using infrared spectroscopy to study thin-section scale microstructures. ATR-IR spectroscopy of serpentinite samples from the Shiraga area, central Shikoku, SW Japan, reveals clear spectral differences between antigorite, chrysotile and lizardite in the 650–1250 cm^{-1} absorbance region associated with the vibration of the Si-O bonds in SiO$_4$ tetrahedra as well as in the 3300–3750 cm^{-1} absorbance region associated with the vibration of the O-H bond in MgO$_2$(OH)$_4$ octahedra. A data-processing algorithm developed for this study allows the absorbance intensity and wavenumber of a particular absorbance peak to be used to create serpentine mineral phase maps based on the highest intensity Si-O absorbance bands for antigorite, chrysotile and lizardite. This method can be used to map thin section scale serpentinite microstructures, which illustrates the potential of ATR-IR as a relatively un-explored analytical tool in petrological studies. A combination of ATR-IR data and chemical composition data obtained by electron microprobe (EPMA) shows that the wavenumber values of antigorite O-H absorbance band are correlated with the Fe content. The dehydration reactions of serpentine minerals play an important role in the hydrodynamics of the earth's lithosphere, and the new information on serpentine mineral

hydroxyl group behavior obtained by applying the technique outlined in this study are of great potential interest to researchers in a wide range of different fields.

1. INTRODUCTION

Serpentine minerals, antigorite, chrysotile and lizardite, are hydrous sheet silicates that contain approximately ~13 wt% of water. They are the main minerals found in serpentinite rocks, which are metamorphic rocks that are formed when ultramafic rocks are hydrated. Metamorphic reactions of serpentine minerals play a key role in many subduction zone processes. For example, the dehydration of serpentine minerals is thought to trigger partial melting in the subduction zone (Ulmer and Trommsdorff, 1995; Hattori and Guillot, 2003; Rüpke et al., 2004). There is also evidence that fluids released from dehydrating serpentine minerals could be the cause for seismicity occurring in subduction zones at depths of ~50-300 km (Peacock, 2001; Dobson et al., 2002; Hacker et al., 2003; Jung et al., 2004).

Antigorite, chrysotile and lizardite are stable in different metamorphic conditions and their formation is controlled by pressure (P) and temperature (T) conditions, kinetic factors and the composition of the metasomatic fluid (Evans, 2004). In addition, the differing coefficients of friction of serpentine minerals, particularly the low coefficient of friction for chrysotile, can have a significant impact on the faulting behavior of serpentinite rocks (Scholz, 2019). Hence, reliable identification of antigorite, chrysotile and lizardite and microstructural analysis of natural serpentinite samples are an important part of developing a better understanding of the metamorphic processes and fault zone dynamics of serpentinite rocks. However, this kind of research is hindered by a limited range of easy to use methods that can be used to identify antigorite, chrysotile and lizardite in standard petrographic thin sections.

Distinguishing the different serpentinite minerals from each other using a polarizing microscope or an electron microprobe can be challenging due to the similarity of their optical

6

properties and chemical composition. A simplified general chemical formula for serpentine minerals is $X_3Y_2O_5(OH)_4$, where X is most often occupied by Mg and Y by Si. However, natural samples exhibit considerable compositional variation. For example, Mg can be substituted by various cations such as Fe^{2+}, Fe^{3+}, Al, Cr, Mn or Ni and Si by cations such as Al and Fe^{3+} (Moody, 1976; O'Hanley and Dyar, 1993).

Different types of serpentine have slightly different ranges of chemical composition, but there is a large overlap and the main distinguishing feature between serpentine minerals is the crystal structure. The basic structure of all serpentine minerals is composed of sheets of SiO_4 tetrahedra that are covalently linked to a layer of $MgO_2(OH)_4$ octahedra (Evans et al., 2013). In the three main serpentine mineral varieties, sheets of these basic units are stacked and bound together in a specific configuration that forms a distinct crystal structure. Antigorite has a wavy, layered structure in which the orientation of the tetrahedral SiO_4 layers is periodically reversed, whereas chrysotile forms layered tubular structures that give chrysotile its typically fibrous appearance. Lizardite, on the other hand, has a simple, layered structure.

Vibrational spectroscopy methods —Raman and infrared spectroscopy— can be used to identify minerals by observing the characteristic molecular vibrations of the different functional groups. Raman and infrared spectroscopy are complementary methods, which means that vibrational modes that are infrared active cannot be Raman active and vice versa. Several studies have documented the characteristic Raman spectra of antigorite, chrysotile and lizardite (e.g., Rinaudo et al., 2003; Enami, 2006) However, Raman spectroscopy of serpentine minerals is affected by fluorescence effects (Groppo et al., 2006), which can make mineral identification more difficult.

Several previous studies (e.g., Farmer, 1974; Post and Borer, 2000; Šontevska et al., 2007) also describe the infrared spectra of serpentine minerals. Nearly all of these studies are conducted using transmission IR spectroscopy. Transmission IR spectroscopy requires samples

to be either ground into a fine powder and pressed into discs, thus losing microstructural information, or made into double polished thin sections of a specific thickness. For serpentine minerals, the double-polished thin section needs to be thinner than about 20 micrometers for a successful measurement. Preparation of such samples is technically challenging and time consuming.

Attenuated total reflection infrared (ATR-IR) spectroscopy is an alternative IR method, which utilizes an ATR crystal, also known as an internal reflection element (IRE), that allows measurements to be made directly from the surface of a normal polished thin section, which greatly reduces the time needed for sample preparation. We studied the suitability of the ATR-IR method to distinguish antigorite, chrysotile and lizardite from samples collected from serpentinite bodies in the Shiraga region of the Sanbagawa metamorphic belt. We also applied the ATR-IR method to map areas with multiple mineral phases in order to demonstrate the possibilities of this technique in analyzing thin section scale microstructures.

2. GEOLOGY OF THE SHIRAGA AREA

Samples analyzed for this study are from the Shiraga area, which is located in the Sanbagawa metamorphic belt in central Shikoku, SW Japan (Fig. 1). The Sanbagawa belt is a high $P–T$ metamorphic belt that runs discontinuously across SW Japan from the tip of Kyushu to the Kanto mountains in the western side of Tokyo (Wallis and Okudaira, 2016). The Shiraga area consists mainly of pelitic, siliceous and mafic schists, which are metamorphosed oceanic sedimentary deposits. Peak metamorphism in the Sanbagawa belt occurred during the Cretaceous (e.g. Endo et al., 2009; Wallis et al., 2009) and metamorphism reached eclogite facies conditions. Omphasite- and jadeite-bearing sedimentary units are also found in the vicinity of the Shiraga area (e.g. Kouketsu et al., 2010; Taguchi and Enami, 2014). There are also several serpentinite bodies in central Shikoku, which are present only in the higher

pressure parts of the Sanbagawa belt (Aoya et al., 2013), suggesting that the serpentinites originate from the mantle wedge. A Recent study by Kouketsu et al. (in print) on the thermal structure of the Asemigawa and Shiraga regions, conducted using the Raman carbonaceous material thermometry, found that the Shiraga area serpentinites are indeed present only in the 430-500 °C region of the Sanbagawa belt further supporting the notion that the serpentinites in the Shiraga area are of mantle wedge origin. A detailed study on the Shiraga area serpentinite bodies by Kawahara et al., (2016), concluded that the protolith of the serpentinite bodies was dunitic but that the ultramafic rocks in the area have since been completely serpentinized. There seems to have been several stages of serpentinization and serpentinite breakdown in the Shiraga area. For instance, most of the Shiraga area serpentinite samples contain some metamorphic olivine, indicating that the metamorphic temperatures experienced by the serpentinites rose above ~640 °C, which is the upper limit of antigorite stability (Evans et al., 2013). In addition, Kawahara et al. (2016) observed an almost monomineralic antigorite-rich region on the eastern boundary of the largest serpentinite body in the Shiraga area and the the pelitic schists, which suggests an inflow of silica-rich fluids from the pelitic schists, which caused the re-serpentinization of the already partially dehydrated serpentinites. In addition to antigorite, which is the main serpentine mineral in the Shiraga region, we also identified numerous samples with lower temperature serpentine minerals, lizardite and chrysotile, which are thought to have formed during exhumation. This study focuses on describing the ATR-IR spectra of antigorite, lizardite and chrysotile from the serpentinite samples from the Shiraga area as well as demonstrating how to apply the ATR-IR method to study serpentinite microstructures.

3. METHODS

3.1. Attenuated total reflection infrared (ATR-IR) spectroscopy

The ATR-IR spectra was measured with a Fourier transform infrared (FTIR) spectrometer (Nicolet iS10 by Thermo Fisher Scientific), which was equipped with a mercury cadmium telluride (MCT) detector at the Petrology Laboratory at Nagoya University. The FTIR spectrometer was attached to an infrared microscope (Nicolet Continuum by Thermo Fisher Scientific) and the instrument was purged with dry air and cooled with liquid nitrogen. The measurements were made using an ATR crystal made of germanium with an angle of incidence of 28° and refractive index of 4. The individual measurements were made from thin sections polished by diamond paste (grainsize 1 μm). The thin sections used for mapping were further polished using colloidal silica. 100×100 μm aperture, which corresponds to a 25×25 μm spot size, was used for the ATR-IR measurements. 32 scans were recorded for each individual measurement. The step size for ATR-IR mapping varied between 25-50 μm. To limit the mapping time, only 16 scans were recorded for each measurement during the ATR-IR mapping. A spectral range of 650–4000 cm^{-1} was recorded with a 4 cm^{-1} resolution for all ATR-IR measurements.

3.2. Raman spectroscopy

The Raman spectra of antigorite grains was measured with a Thermo Fisher Scientific Almega XR Raman micro-spectrometer using gratings of 2400 lines/mm. The instrument is equipped with a 532 nm Nd-YAG laser, a CCD-detector (256×1024 pixels), and an automated Olympus BX51 confocal microscope. The objective lens used was Olympus Mplan-BD 100X (numerical aperture; NA=0.90). Frequencies of the Raman bands were calibrated by monitoring the position of a plasma line from the Ne laser (703.241 nm). Raman spectra for each grain of antigorite were measured in both the low wavenumber range (100–1286 cm^{-1}) and high wavenumber range (3387–4087 cm^{-1}). The acquisition duration was 60 s divided into six accumulating cycles. The peak position of the Raman spectrum was calibrated using the 520

cm^{-1} band of a Si-wafer. The temperature of the analytical room was maintained at 20 °C during measurements.

3.3. Electron microprobe (EMPA)

The chemical compositions of the serpentine minerals were analyzed quantitatively by wavelength-dispersive spectrometer (WDS) by an electron probe microanalyzer (JXA-8900R; JEOL) at the Petrology Laboratory of Nagoya University. The accelerating voltage of individual quantitative measurements was set to 15 kV with a 12 nA beam current and a 5 μm beam spot diameter. For mapping, the accelerating voltage and the beam current were set to 20 kV and 100 nA, respectively. The step size used for mapping was 5 μm. The correction factors calculated by Kato (2005) were employed for matrix correction.

4. SAMPLE DESCRIPTION

The most common serpentine mineral found in the Shiraga area serpentinite bodies is antigorite. Antigorite is typically platy (Fig. 2a) but it can also have a fibrous appearance. Chrysotile and lizardite were formed after the main antigorite-dominated serpentinization and they are present in a limited number of samples, mostly found between the contact zone of the serpentinite bodies and the surrounding metasedimentary rocks. The chrysotile veins in the Shiraga area serpentinites are characteristically fibrous (Fig. 2b). Lizardite is fine-grained and is found in anastomosing veins, which appear reddish (Fig.2c) due to the presence of iron-oxides. Several samples also contain all three serpentine minerals (Fig. 2d). These samples are especially interesting as they contain reaction textures between the serpentine minerals, which can be studied in detail using infrared spectroscopy. In addition to the three serpentine minerals, the samples also contained olivine (of metamorphic origin), magnetite, Cr-spinel and brucite as well as some other minor accessory minerals, such as talc. The preliminary mineral identification of serpentine minerals was made by Raman spectroscopy using the characteristic

Raman peaks proposed by Enami (2006). Figure 3. shows representative Raman spectra of antigorite, chrysotile and lizardite. These measurements were made from the same samples as the representative ATR-IR spectra for each respective serpentine mineral.

5. RESULTS

5.1. ATR-IR spectra of serpentine minerals

In order to select representative spectra of antigorite, chrysotile and lizardite, we chose 30 ATR-IR measurements (10 measurements of each mineral) and determined the wavenumber value of each absorbance band using the spectral peak fitting software PeakFit 4.12. From these 30 measurements, we chose the most representative spectra of antigorite, chrysolite and lizardite to present in this study (Fig. 4). The measurement locations of the representative ATR-IR spectra of antigorite, chrysotile and lizardite are shown in Figure 2. All three serpentine minerals have two dominant vibrationally active domains in their crystal structure, which can absorb radiation in the mid-infrared range that was measured for this study (650–4000 cm^{-1}). Exact wavenumber values of all absorbance bands that were detected are listed in Table 1 along with results from previous IR studies of serpentine minerals made using the transmission IR method.

The lower wavenumber region (650–1250 cm^{-1}) is associated with the vibration of the Si-O bonds in the SiO_4 tetrahedra of serpentine minerals (Deer et al., 2009). The biggest difference between the three serpentine minerals in the low wavenumber region is the position of the highest intensity absorbance band. The highest intensity absorbance bands of antigorite, chrysotile and lizardite are at ~959 cm^{-1}, ~941 cm^{-1}, ~930 cm^{-1}, respectively. In addition, antigorite has several low-intensity peaks in the low wavenumber region (650–1250 cm^{-1}), which are not present in the ATR-IR spectra of chrysotile and lizardite. These absorbance

bands are related to various lower energy Si-O vibrational modes (Šontevska et al., 2007) caused by the complex undulating crystal structure of antigorite.

The high wavenumber region (3300–3750 cm^{-1}) is associated with the vibration of the O-H bond in the $MgO_2(OH)_4$ octahedra. The largest difference between the serpentine minerals in this region is in the intensity of the absorbance and the overall number of absorbance peaks. In addition to the main O-H absorbance peak at 3671 cm^{-1}, antigorite has four subsidiary low-intensity peaks in the 3300–3750 cm^{-1} region. Mellini et al. (2002) suggest the main O-H peak of antigorite peak is related to the inner O-H stretching and that the lower wavenumber peaks are related to variations in the O-H bond strength, which can be caused by octahedral substitutions of Mg by other cations. The chrysotile spectrum in the high wavenumber region is characterized by two peaks at ~3680 cm^{-1} and ~3643 cm^{-1}, which are related to the inner and outer stretching vibrations of the O-H bond (Viti and Mellini, 1997). The 3300–3750 cm^{-1} region of lizardite is characterized by a sharp main absorbance peak at 3683 cm^{-1}, which is also thought to be related to the in-phase vibrations of O-H groups (Balan et al., 2002a).

5.2. Chemical compositions of serpentine minerals

The chemical compositions of the representative antigorite, chrysotile and lizardite are shown in Table 2. Antigorite is enriched in silicon in comparison to chrysotile and lizardite. This is because the crystal structure of antigorite can accommodate slightly more silicon due to the periodic reversals of the SiO_4 tetrahedra in antigorite (Evans et al., 2013). Other small compositional differences that we observed are: the higher aluminum content of chrysotile and the higher iron content of lizardite, which might be partly caused by the iron-oxides in the lizardite veins. These compositional variations are within the limits of regular serpentine mineral compositions published previously (e.g., Brindley and Wan, 1975; Peacock, 1987).

5.3. ATR-IR mapping

In order to study the variation in the ATR-IR spectra of serpentine minerals in more detail, we developed an algorithm to process the ATR-IR mapping data. The algorithm uses the 'findpeaks' function, available in many data-processing software, to determine the wavenumber value and intensity of the highest intensity absorbance band in a certain region of the ATR-IR spectra (Figs. 5a and 5b). A detailed description of the algorithm as well as how to apply it in the field of vibrational spectroscopy is given in the 3rd chapter of this thesis.

The algorithm developed for this study makes it possible to create serpentine mineral phase maps since each serpentine mineral has a characteristic highest intensity Si-O absorbance band (Fig. 6). In addition to antigorite, chrysotile and lizardite, the ATR-IR map of sample KSY71 (Fig. 6), also contains a significant amount of olivine and some magnetite. The highest ATR-IR absorbance peak of olivine is at ~866 cm^{-1} and it is included in the calculations (Fig. 5a). Magnetite does not have a distinct absorbance band in the mid-infrared range measured for this study (Chamritski and Burns, 2005) so the locations with magnetite are left blank in Figures 6 and 7.

Furthermore, it is possible to use ATR-IR mapping to examine spectral variation of a single mineral. In order to illustrate this, we mapped a serpentinite sample KSY75 from the Shiraga area, which contains antigorite veins running through an antigorite matrix (Fig. 7a). In sample KSY75, the wavenumber values of the highest intensity O-H absorbance bands vary between the veins and the matrix (Fig. 7b). The wavenumber values of the O-H absorbance bands of antigorite grains in the matrix are between 3660 and 3666 cm^{-1}, while the antigorite grains in the veins tend to show higher values between 3666 and 3670 cm^{-1}. To see if the differences in the wavenumber values of O-H absorbance bands are caused by variation in the chemical composition, we mapped the chemical composition of sample KSY75 using an electron microprobe. We measured the distribution of Si, Al, Mg, Fe, Mn, Cr, Ni and Ti in the sample and found that variations in the Fe concentration (Fig. 7c) correlated with variations in

the O-H absorbance values of antigorite (Fig. 7b). Quantitative microprobe analyses show that Fe contents of antigorite range from 0.05 to 0.09 pfu with lower concentrations in the veins than in the matrix (Fig. 7d).

6. DISCUSSION

The ATR-IR method has proven to be a simple and reliable method to measure the infrared spectrum of serpentine minerals. There are clear differences between the three serpentine minerals in the wavenumber values and overall shape of the spectra (Fig. 4). For example, the highest intensity absorbance bands of antigorite, chrysotile and lizardite have characteristic values of ~959 cm^{-1}, ~941 cm^{-1} and ~930 cm^{-1}, respectively. The differences observed between the highest intensity absorbance bands of the three serpentine minerals are because of different Si-O bond energies, which are due to varying bond lengths related to the contrasting crystal structures of different serpentine minerals (Mellini et al., 2002).

Most of the ATR-IR absorbance bands of serpentine minerals observed in this study are in good agreement with previously published studies (Table 1). A larger number of low-intensity bands in the ATR-IR spectra were detected in this study than in some of the previous transmission IR studies. This could be because it is difficult to distinguish lower absorbance peaks from background noise or simply because previous workers catalogued their observations in a different way. The high-intensity absorbance bands in the transmission IR spectra tend to have higher wavenumber values than the high-intensity ATR-IR absorbance bands. For instance, in the transmission IR studies, the highest intensity absorbance band of antigorite has a wavenumber value nearly 30 cm^{-1} higher than the corresponding band observed in the ATR-IR spectra. The differences in the serpentine mineral absorbance band positions observed between the ATR-IR measurements and the previously published transmission IR studies are caused by the different ways in which light interacts with the sample in the different

infrared spectroscopy methods. Spectral distortions are common in transmission IR measurements made using KBr pellet samples because electrostatic interactions between different particles in a powdered sample influence the whole macroscopic electric field of the sample (Balan et al., 2011). The ATR-IR method is also susceptible to spectral distortions, because the difference in refractive indices of the sample and the ATR crystal causes anomalous dispersion of infrared radiation at the interface between the crystal and the sample resulting in shifts of the spectral peaks (Woods and Bain, 2014). This means that the ATR-IR spectra of serpentine minerals will be slightly different when measurements are made with ATR crystals with different refractive indices.

This study highlights some of the difficulties faced when trying to distinguish different serpentine minerals from each other using a polarizing microscope and how ATR-IR mapping can resolve some of these issues. For example, in the thin section image of sample KSY71 (Figure 6a) both lizardite and antigorite show similar discoloration by iron-oxides and there is no clear contrast in the associated crystal habits meaning that the boundary between these two minerals is unclear. However, an overlay of the ATR-IR map on the thin section image (Figure 6c) clearly reveals the location of the boundary. The inverse situation can also be observed. The boundary between chrysotile and lizardite appears sharp in the thin section image of sample KSY71 (Figure 6a). However, the ATR-IR map reveals the presence of a boundary zone between the two domains with a symplectitic intergrowth of lizardite and chrysotile (Figure 6b). On closer inspection, symplectitic intergrowths can also be observed in some other sections of the boundary between chrysotile and lizardite (Figure 6a). Intergrowths such as these in serpentine minerals have been previously reported (Bailey and Banfield, 1995; Dódony and Buseck, 2004) and the ATR-IR technique offers a simple way to recognize and image them. It should be also noted that although coloration and other features may allow different types of serpentine minerals to be distinguished under the polarizing microscope, these features are not

consistent between different samples and some other method, such as that proposed here, is required to identify the particular mineral species.

Other factors that can affect the observed infrared spectra are variations in crystallographic orientation and compositional changes. Balan et al. (2002b) studied the effect of crystallographic orientation on the ATR-IR spectra of chrysotile. According to their observations the wavenumber value of the highest intensity absorbance peak of chrysotile varied between 938-957 cm^{-1} depending on the crystallographic orientation. Such large variation was not observed in this study, perhaps suggesting that chrysotile in our sample has a strong crystallographic preferred orientation.

Studying variations in serpentine mineral O-H absorbance bands is of interest to many researchers as it can further our understanding of the hydration and dehydration reactions of serpentinites. Figure 7 illustrates how changes in chemical composition can affect the O-H absorbance bands of antigorite. A comparison between the ATR-IR map of O-H absorbance band values of antigorite and the EMPA map of Fe distribution, shows a close correspondence (Figs. 7b and 7c). High iron content (~0.09 pfu) regions have up to 10 cm^{-1} lower O-H absorbance values than low iron content (~0.05 pfu) regions (Figs. 7b and 7d). This observation is in line with the suggestion made by Mellini et al. (2002) that the octahedral substitution of Mg by Fe^{2+} would shift the main O-H absorbance band of antigorite to lower wavenumbers. Other elemental substitutions, for example Si by Al, have also been observed to have a significant impact on the IR spectra of serpentine minerals (e.g., Serna et al., 1979; Velde, 1980). However, no other clear correlations between the ATR-IR and EMPA maps were observed in this study.

While ATR-IR maps of individual absorbance bands are useful in illustrating spectral variations and studying their connection to serpentinite microstructures, it is better to examine the whole serpentine mineral spectrum when making a mineral identification. As mentioned

before, the intensities and wavenumber values of individual absorbance bands can be affected by several factors, such as variations in mineral microstructure, crystallographic orientation and chemical composition and more work is necessary to study how such factors affect the ATR-IR spectra of serpentinite minerals.

7. CONCLUSIONS

This study shows that the ATR-IR method is well suited to the *in situ* identification of serpentine minerals. The ease of making measurements directly from the surface of a thin section means the ATR-IR method has a considerable as yet largely un-explored potential in the field of mineral spectroscopy. This study also demonstrates that using a data-processing algorithm can be useful in teasing out small-scale fluctuations in absorbance intensities and wavenumber values of individual absorbance peaks in large ATR-IR mapping datasets. This kind of more quantitative approach revealed that the Fe concentration can have a noticeable effect on the wavenumber values of antigorite O-H absorbance bands. More detailed ATR-IR mapping of serpentinite microstructures, such as veins or fault structures, in combination with other petrological methods, such as EPMA and EBSD mapping, can further improve our knowledge of the serpentinization processes.
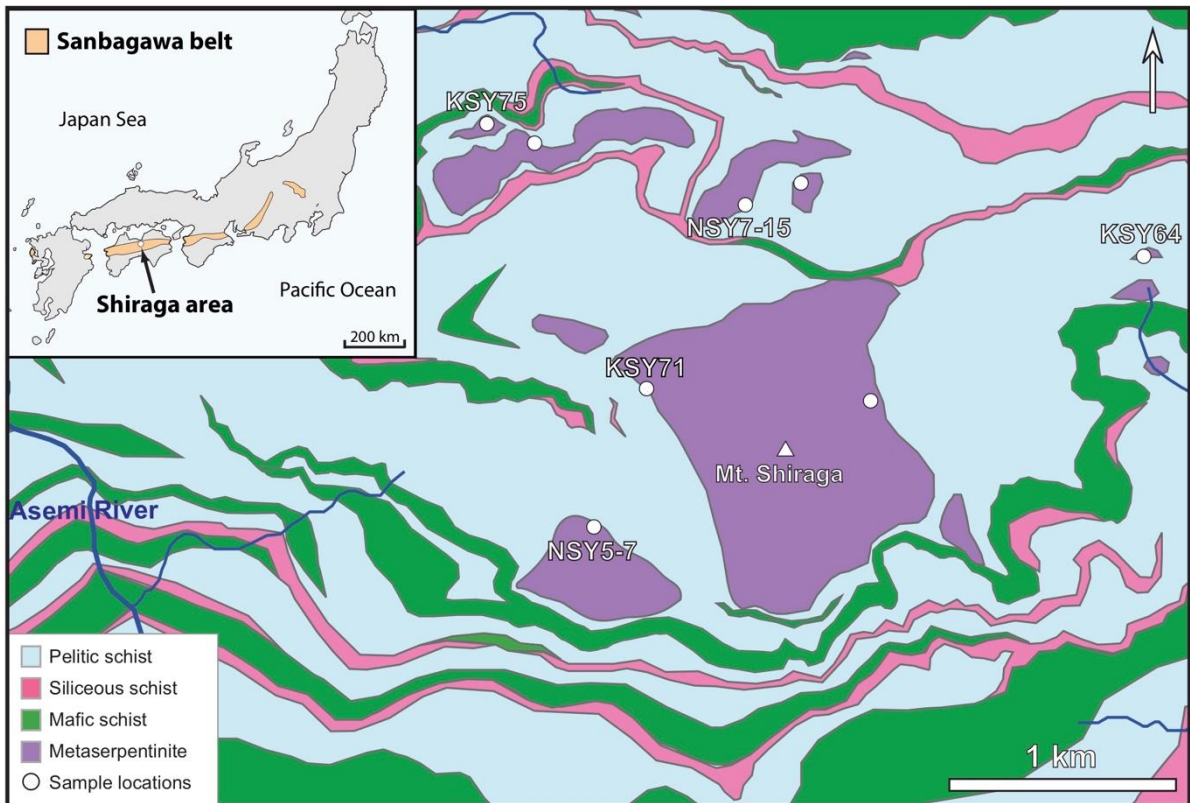
F**igure 1.** Geological map of the Shiraga area and its location in the Sanbagawa metamorphic belt, SW Japan (Modified after Kawahara et al. 2016). Sampling locations of the samples measured for this study are indicated. The sample names of the samples described in more detail in this study are written below the sampling location.
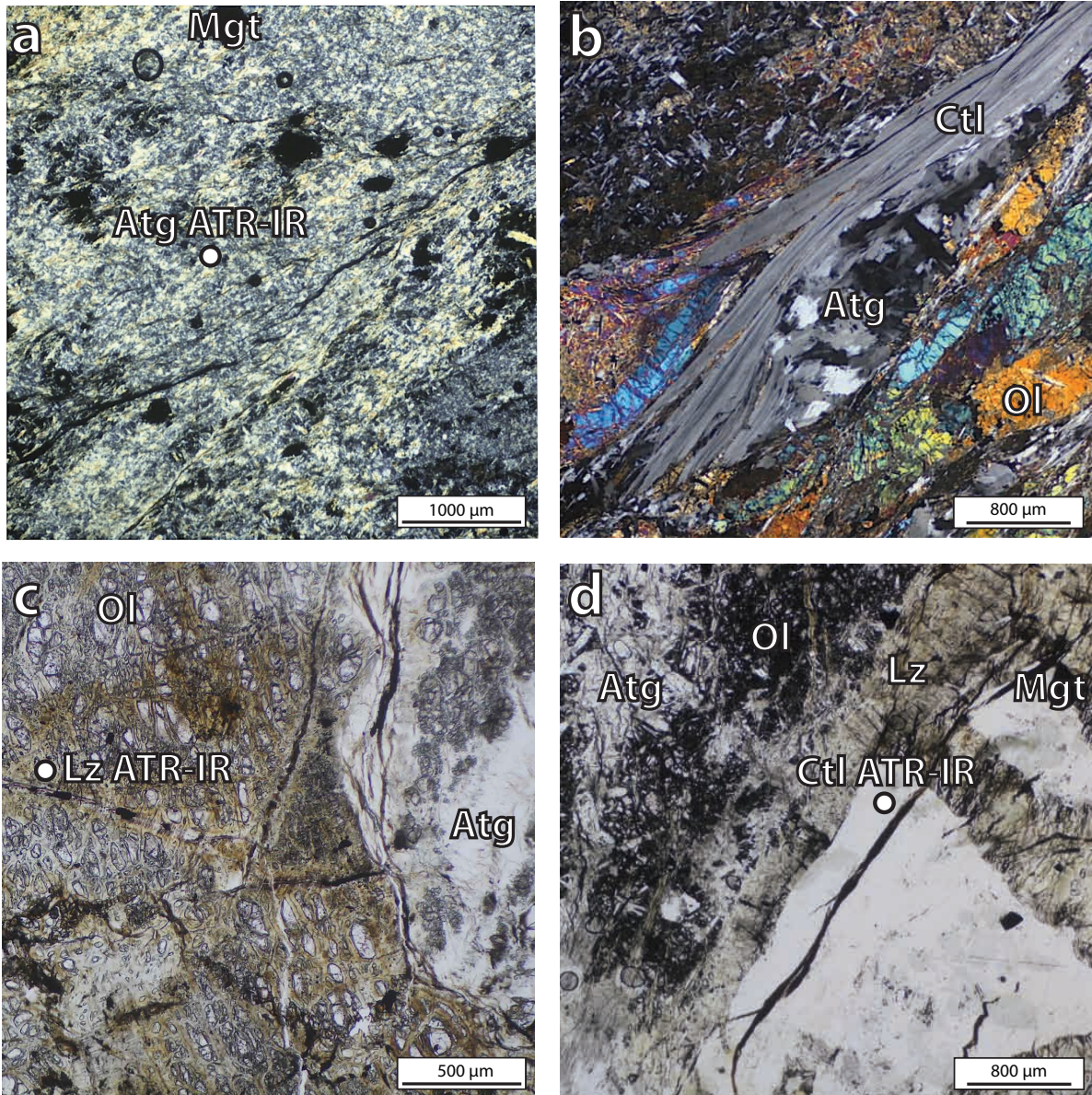
Figure 2. Thin section images of serpentine minerals from Mt. Shiraga serpentinite body taken in cross polarized light (XPL) and plane polarized light (PPL). (a) Antigorite from sample NSY7-15, XPL (b) Chrysotile vein that also contains antigorite in a matrix of antigorite and olivine. Sample NSY5-7, XPL. (c) Iron-oxide stained anastomosing lizardite veins running through a matrix of antigorite, olivine and magnetite. Sample KSY64, PPL. (d) A reaction zone of co-existing antigorite, lizardite and chrysotile with fine-grained olivine and magnetite. Sample KSY71, PPL. Atg, antigorite; Ctl, chrysotile; Lz, lizardite; Ol, olivine; Mgt, magnetite. The measurement locations of the ATR-IR spectra of antigorite, chrysotile and lizardite presented in this study are indicated.
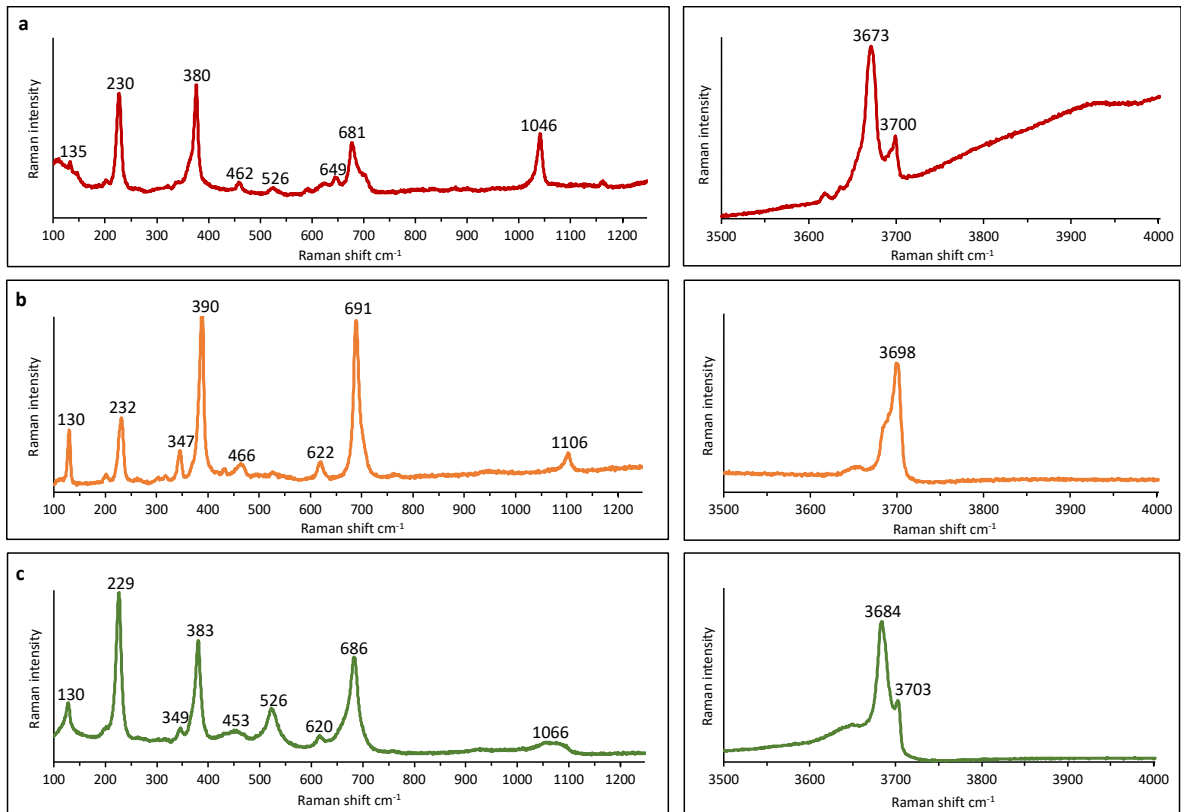
Figure 3. Raman spectra of (a) antigorite from sample NSY7-15, (b) chrysotile from sample KSY71 and (c) lizardite from sample KSY64.
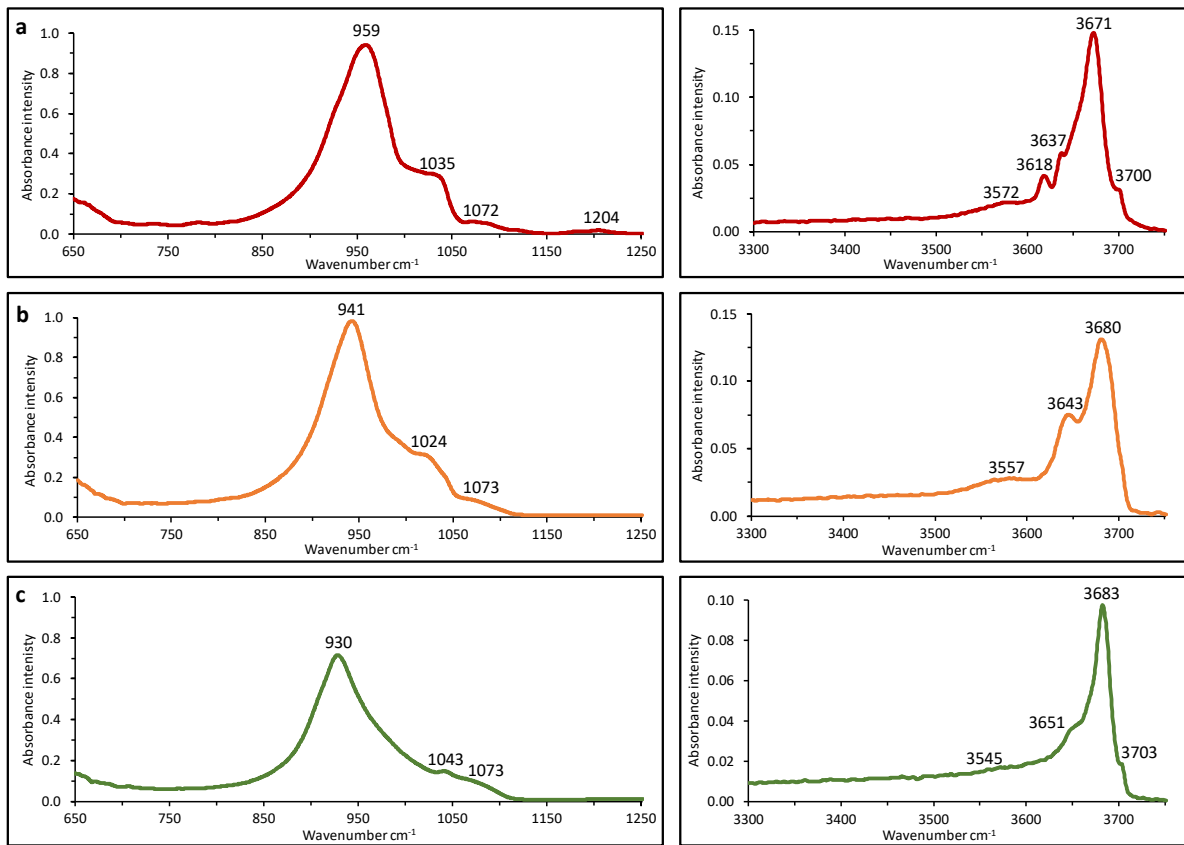
Figure 4. Representative ATR-IR spectra of (a) antigorite from sample NSY7-15, (b) chrysotile from sample KSY71 and (c) lizardite from sample KSY64.
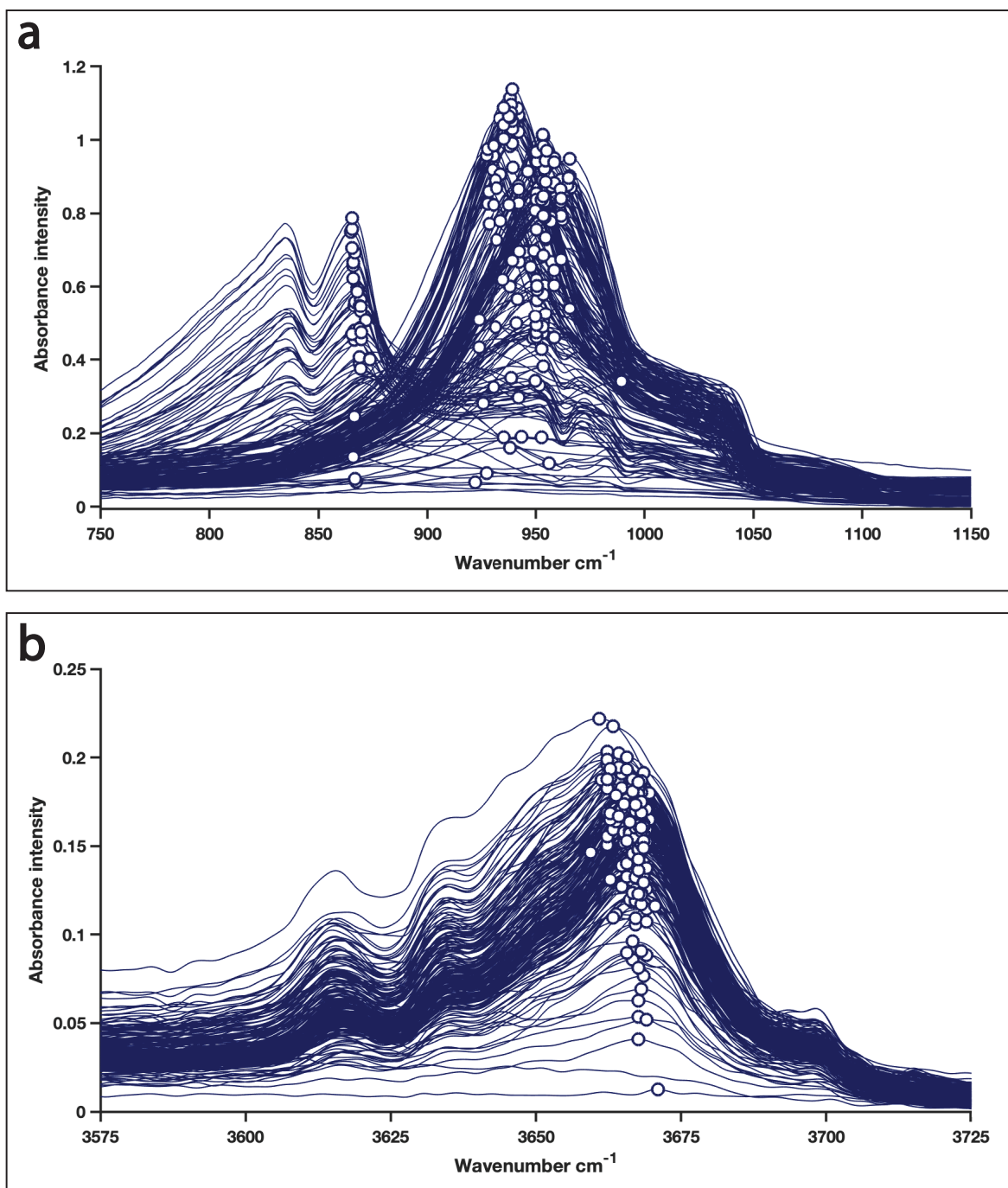
Figure 5. A representative selection of ATR-IR mapping spectra showing a) the 750-1150 cm^{-1} region of sample KSY71 and b) the 3575–3725 cm^{-1} region of sample KSY75. The white areas represent the highest intensity absorbance peaks of each individual measurement in this region as determined by the 'findpeaks' function. The ATR-IR maps made from these datasets for samples KSY71 and KSY75 are displayed in Figures 6 and 7, respectively.
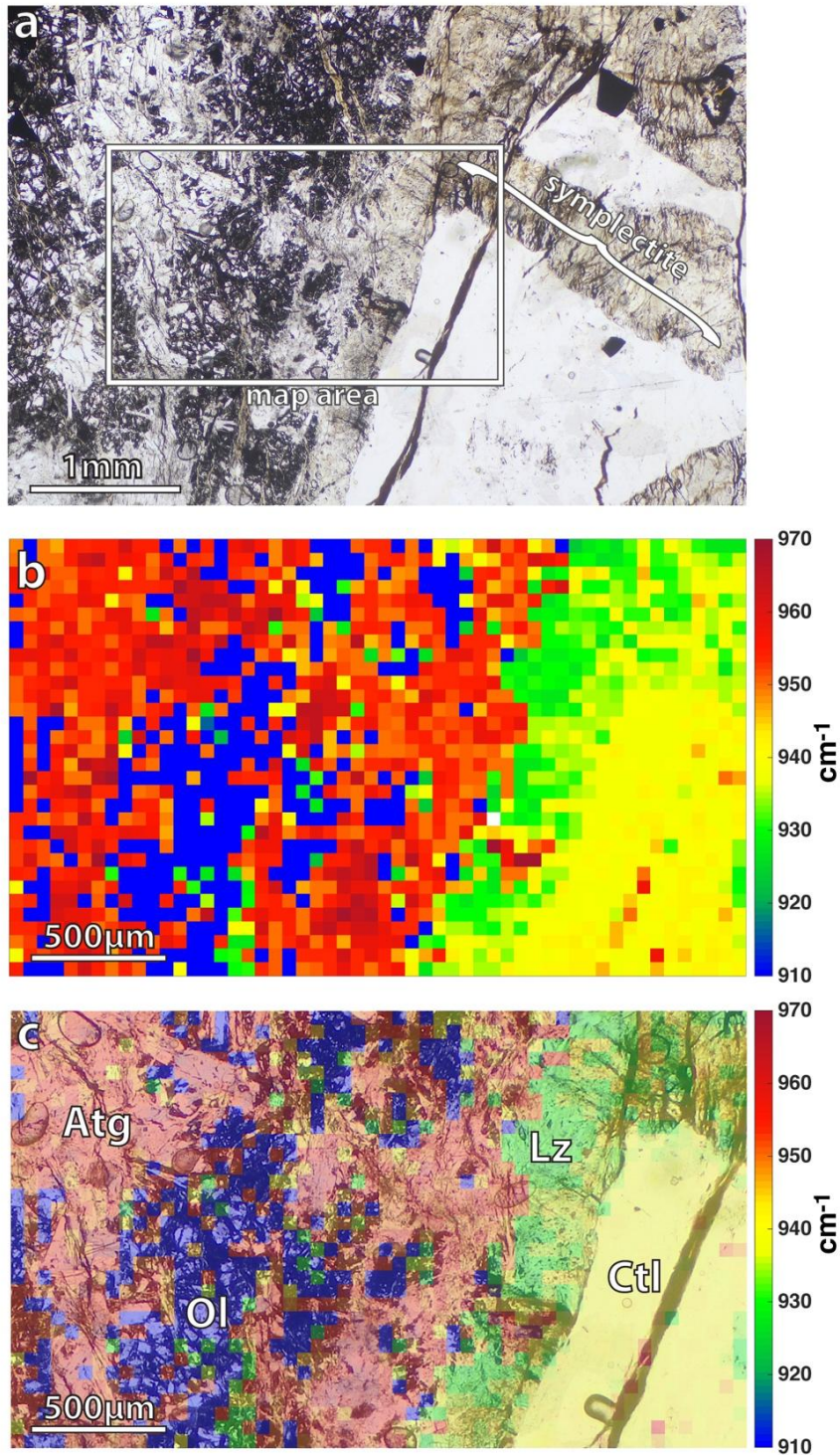
Figure 6. (a) A plane polarized thin section image of sample KSY71. (b) An ATR-IR map of the indicated area in Figure 5a showing the wavenumber values of highest intensity absorbance peaks in the 650-1250 cm^{-1} region. Mapping step size was 50 μm. (c) A comparison between the ATR-IR map of sample KSY71 and a plane polarized thin section image of the mapped area. The sample contains antigorite (Atg; in red areas), chrysotile (Ctl; in yellow areas), lizardite (Lz; in green areas) and olivine (Ol; in blue areas).
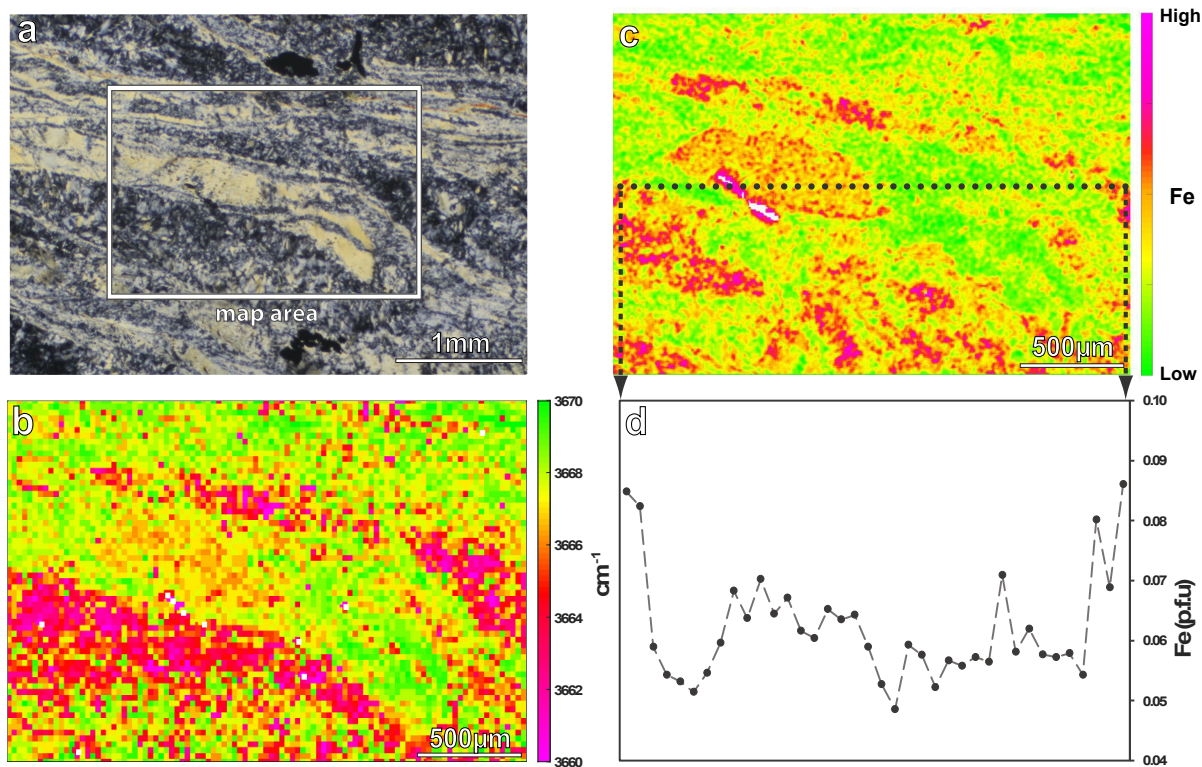
Figure 7 (a) A cross-polarized thin section image of antigorite veins running through an antigorite matrix in sample KSY75. (b) An ATR-IR map of the indicated area in Figure 7a showing the wavenumber values of the highest intensity O-H absorbance bands of antigorite in the 3300–3750 cm⁻¹ region. In addition to antigorite, this map also includes minor amounts of magnetite (white areas). Mapping step size was 25 µm. (c) An EPMA map of relative Fe concentration in antigorite measured from the indicated area in Figure 7a. The original mapping step size was 5 µm, but each pixel in the map is recalculated to show average values from an area of 25x25 µm for the purpose of comparing the relative Fe concentration to the wavenumber values of antigorite O-H absorbance bands. (d) Fe concentrations of antigorite per formula unit (pfu) on the basis of O = 7 from the cross-section indicated in Figure 7c.

Table 1. Representative experimental ATR-IR absorbance band values (in cm^{-1}) of antigorite, chrysotile and lizardite in the mid-infrared region (650-4000 cm^{-1}) in this study and the corresponding transmission IR absorbance band values from previous studies.

Antigorite				
This study	Post and Borer, 2000	Šontevska et al., 2007	Mellini et al., 2002	Farmer, 1974
959	990	987	983	994
1035	1076	1083	1082	1077
1072	-	-	-	-
1204	1202	1205	-	1205
3572	3568	-	3561	-
3618	3620	-	3622	-
3637	3652	-	3637	-
3671	3673	3678	3678	3675
3700	3697	3699	3700	3700
Chrysotile				
This study	Post and Borer, 2000	Šontevska et al., 2007	Anbalagan et al., 2010	Viti and Mellini, 1997
941	958	961	965	956
1024	1068	1078	1079	1072
1073	-	-	-	-
3557	-	-	-	-
3643	3647	3646	3648	3640
3680	3685	3688	3689	3688
Lizardite				
This study	Post and Borer, 2000	Balan et al., 2002a	Mellini et al., 2002	Viti and Mellini, 1997
930	959	948	951	952
1043	1075	1080	1084	1088
1073	-	-	-	-
3545	3558	3584	3585	3586
3651	3653	3645	3651	-
3683	3685	3684	3684	3685
3703	-	3703	3703	-

Table 2. Chemical composition of the representative ATR-IR spectra of antigorite, chrysotile, and lizardite from Mt. Shiraga serpentinite body. Total iron is shown as FeO and Mg# = (Mg/(Mg + Fe)).

Mineral	antigorite	chrysotile	lizardite
Sample	NSY7-15	KSY71	KSY64
SiO_2 wt%	44.27	41.60	39.29
TiO_2	0.00	0.03	0.03
Al_2O_3	0.51	1.63	0.01
Cr_2O_3	0.33	0.38	0.00
FeO	1.04	2.03	3.89
MnO	0.03	0.02	0.08
MgO	40.42	40.18	40.21
NiO	0.14	0.08	0.25
Total	86.75	85.95	83.75
Numbers of ions on the basis of O = 7			
Si	2.05	1.96	1.94
Ti	0.00	0.00	0.00
Al	0.03	0.09	0.00
Cr	0.01	0.01	0.00
Fe	0.04	0.08	0.16
Mn	0.00	0.00	0.00
Mg	2.79	2.83	2.95
Ni	0.01	0.00	0.01
Sum cation	4.93	4.98	5.06
Mg#	0.986	0.972	0.949

Part 2:

The microstructure and composition of antigorite serpentinites from the high-*P*

metamorphic Yuli Belt in eastern Taiwan

ABSTRACT

Antigorite is a hydrous mineral and the main component of subduction zone serpentinites. The fluids released by serpentinite dehydration reactions play an important role in many subduction zone processes, such as in elemental cycling, melt formation and in causing hydrofracturing in the subduction zone, which can make certain regions of the subduction zone more susceptible to seismic activity. However, the wide stability field of antigorite and the almost monomineralic composition of serpentinites make it challenging to study the metamorphic processes of subduction zone serpentinites in detail. In this study, we analyzed various microstructures and compositional variation of three serpentinite bodies located in the Yuli Belt, a high pressure metamorphic belt in eastern Taiwan, to see if the composition and microstructure of antigorites varied in different parts of the Yuli Belt and if those changes could be connected to the metamorphic history of the surrounding region. The microstructure of the samples was studied using optical microscopy and attenuated total reflection infrared spectroscopy (ATR-IR) and the composition of the samples was measured by electron microprobe analyzer (EPMA). Based on our analyses, we found that the Yuli belt serpentinites were subjected to active fluid flow during subduction. Measurements from different alteration zones and veins showed that antigorite was recrystallized by several pulses of fluid flow. Especially the Fe content of antigorite varied between the samples and this was reflected also in the ATR-IR spectrum of the antigorites.

1. INTRODUCTION

Serpentinite is an important component of the subducting oceanic lithosphere as well as the mantle wedge. In particular, the hydration and dehydration reactions of serpentine minerals have a major impact on the hydrodynamics of the subduction zone. Serpentinites in the subduction zone are largely made up of antigorite (Atg), a high temperature serpentine variety. The metamorphic reactions of Atg-serpentinites are linked to processes such as subduction zone melt formation (Hattori and Guillot, 2003; Rüpke et al., 2004; Ulmer and Trommsdorff, 1995) and elemental cycling (Alt et al., 2013; Peters et al., 2017; Scambelluri et al., 2019). Many researchers also believe that fluids released by antigorite dehydration could be the cause for seismicity occurring in subduction zones at intermediate depths (~50-300 km) (Peacock, 2001; Dobson et al., 2002; Hacker et al., 2003; Jung et al., 2004).

A simplified general chemical formula for antigorite is $X_3Y_2O_5(OH)_4$, where X is usually occupied by Mg and Y by Si. The crystal structure of antigorite is comprised of MgO octahedra that are linked to Si-O tetrahedra. The orientation of the Si-O tetrahedra is periodically reversed giving antigorite a wavy structure. The number of Si-O tetrahedra along a half wave *a* in the antigorite crystal structure is called the m-value and the ideal antigorite structure has an m-value of 17. Antigorite can be formed by metamorphic reactions of lizardite and chrysotile bearing abyssal serpentinites, which are subjected to high pressure (*P*) and temperature (*T*) conditions during subduction or by primary serpentinization of mantle wedge peridotites. The stability of antigorite is mostly controlled by temperature and in a pure MgO–SiO_2–H_2O system antigorite is considered stable at 2 GPa in temperatures of ~320-640 °C (Evans et al., 2013). However, experimental studies of natural antigorite serpentinites have shown that antigorite can be stable up to temperatures of 650-710 °C in 1.5-1.9 GPa (Padrón-Navarta et al., 2010; Trommsdorff et al., 1998). This is due to compositional and structural variation of antigorite, both of which have a significant effect on the stability of antigorite.

Hence, several workers have turned their attention to studying the microstructure and composition of antigorite in order to accurately understand the metamorphic processes of serpentinites. For example, previous studies (Mellini et al. 1987; Wunder et al. 2001) suggest that the m-value of antigorite might be partially dependent on P–T conditions. Also, it has been shown that higher Al concentration can make antigorite more stable in higher temperatures (Bromiley and Pawley, 2003; Padrón-Navarta et al., 2013). Furthermore, it has been observed that an increase in Fe content will lower antigorite dehydration temperatures (Bretscher et al., 2018; Merkulova et al., 2016)

In this study, we investigated the microstructure and composition of serpentinites collected from the high-P Yuli belt in eastern Taiwan to see if observations made from antigorite crystals, measured from samples with various microstructures and mineral assemblages, contained systematic variations that could be linked to the metamorphic conditions previously reported from Yuli belt. The microstructure of antigorites was studied using optical microscope and attenuated total reflection infrared (ATR-IR) spectroscopy and the composition was measured using electron microprobe analyzer (EPMA).

2. GEOLOGY

2.1. Tectonic history of the Yuli Belt

The Yuli belt is a high-pressure metamorphic belt in eastern Taiwan (Fig 1). It is part of the Tananao schist complex, which is comprised of two metamorphic belts: (1) the high T/Low P Tailuko (or Taroko) belt and (2) the high P/Low T Yuli belt (Byrne et al. 2011). The Tananao schists are interpreted to represent the remnants of a late Cenozoic subduction complex, which formed during the subduction of the South China Sea plate. To the east, the Yuli belt in bounded by the Longitudinal Valley, a suture zone filled with tertiary sediments, and the Costal Range, a mountain range which was formed when the Luzon arc collided with the European

continental margin. It has been proposed (Sandmann et al., 2015; Yui et al., 2014) that the rocks in Yuli belt were uplifted to the surface during this collision ~2-5 Ma, making Yuli belt one of the youngest exposed high-*P* metamorphic belts in the world. Peak metamorphic pressures and temperatures, determined by pseudosection modelling of glaucophane-bearing rocks in the Yuli belt, were estimated to have reached between 10–13 kbar and 530-560 °C, respectively (Baziotis et al., 2017). The maximum depth of subduction estimated by Baziotiset et al. (2017) is ~40-45 km, indicating that Yuli belt has a relatively cold geothermal gradient.

2.2. Yuli Belt serpentinites

Most of the Yuli Belt consist of pelitic and psammitic quartz-mica schists but there are also several occurrences of mafic and ultramafic rocks, such as metabasites, greenschists, chlorite schists and serpentinites. There are four main serpentinite localities in the Yuli Belt; the Fengtien, Wanjung, Juisui and Chinshuichi (also known as Yuli) regions (Fig. 2a). According to the preliminary conclusions of Dewangga (2019), who studied the Cr-spinel compositions of Juisui and Fengtien serpentinites, the Yuli belt serpentinites appear to originate from the subducting slab.

For this study, we conducted field surveys and collected samples from the Wanjung, Juisui and Chinshuichi regions. The serpentinite rocks in the Wanjung region (Fig 2b) are located in a block of metabasites consisting of serpentinites, meta-gabbroes and epidote amphibolite, which are surrounded by quartz-mica schist and greenschist (Lin, 1999; Liou, 1981). The Wanjung block serpentinites are associated with omphacite-bearing rocks (Yui and Lo, 1989), suggesting that the rocks in this region underwent high-pressure blueschist facies metamorphism. The serpentinite outcrops in the Wanjung region are heavily weathered and covered by thick undergrowth (Fig. 3a), which makes detailed structural observations challenging.

There are several serpentinite bodies in the Juisui region of Yuli Belt. In most of the Juisui region, serpentinite bodies are surrounded by graphite-bearing quartz-mica schists. However, occurrences of serpentinite can also be found in the Tamayen tectonic block (Fig. 2a), which is made up of mostly greenschist/chlorite schist, with smaller occurrences of epidote-amphibolite, metabasites, and as well as some rare high-P glaucophane schist, which have been used to determine the peak metamorphic conditions in the Yuli Belt (Baziotis et al., 2017; Tsai et al., 2013). The samples from the Juisui region described in this study are collected from Mt. Tsunkuan serpentinite body (Fig. 2c), located within the Juisui unit of the Yuli belt. The Mt. Tsunkuan serpentinite body is made up of mostly antigorite serpentinite along with some minor accessory minerals, such as magnetite and magnesite. There is an approximately ~10 m wide mineralogically complex alteration zone between the serpentinite body and the pelitic schists. This contact zone is rich in chlorite, talc, epidote, amphibole and albite as well as a wide range of more minor accessory minerals, such as pyrite, ilmenite, apatite and zircon (Dewangga, 2019). The inner parts of the serpentinite body are more massive and display brecciated structures (Fig. 3b). Many samples collected from the inner parts of the serpentinite body contained abundant magnesite. In addition, we observed several fibrous antigorite veins, the largest one being ~2 cm thick (Fig 3c).

Serpentinite bodies in the Chinshuichi region are associated with the Chinshuichi mélange, which comprises of graphite-bearing quartz mica schists and chlorite schists and a mixture of serpentinite, pillowed metabasaltic rock, epidote–amphibolite and meta-plagiogranite (Fig. 2d) (Keyser et al., 2016). The serpentinite bodies are mostly massive and are characterized by brecciated structures similar to those in the Juisui region. The characteristic feature of the serpentinites in the Chinshuichi region is the large amount of magnetite clusters (Fig. 3d). The serpentinite is cross-cut by various types of veins, such as thin magnesite veins. The contact zone of the serpentinite and the pelitic schist also contains

thick, 10 cm scale, talc veins (Fig. 3e). The talc rich contact zone is lighter in color than the inner parts of the serpentinite body and the samples contain less magnetite. We also observed a large 15 cm wide rodingite vein (Fig. 3f) made up of garnet and chlinochlore. The rodingite vein contains miarolitic cavities, suggesting that it was formed quite late during the exhumation process when the rocks were under less pressure.

3. METHODS

3.1. Attenuated total reflection infrared (ATR-IR) spectroscopy

The ATR-IR spectra of antigorites was measured with a Fourier transform infrared (FTIR) spectrometer (Nicolet iS10 by Thermo Fisher Scientific) equipped with a mercury cadmium telluride (MCT) detector at the Petrology Laboratory at Nagoya University. The FTIR spectrometer was attached to an infrared microscope (Nicolet Continuum by Thermo Fisher Scientific) and the instrument was purged with dry air and cooled by liquid nitrogen. The measurements were made using a germanium ATR crystal with an angle of incidence of 28° and refractive index of 4. The individual spot measurements were made from thin sections polished by diamond paste (grainsize 1 μm). 100×100 μm aperture, which corresponds to a 25×25 μm spot size, was used for the ATR-IR measurements. A spectral range of 650–4000 cm^{-1} was recorded with a 4 cm^{-1} resolution for all ATR-IR measurements. 32 scans were recorded for each individual measurement.

3.2. Electron microprobe (EMPA)

The compositions of the serpentine minerals were analyzed quantitatively by wavelength-dispersive spectrometer (WDS) by an electron probe microanalyzer (JXA-8900R; JEOL) at the Petrology Laboratory of Nagoya University. The accelerating voltage of individual quantitative

measurements was set to 15 kV with a 12 nA beam current and a 5 μm beam spot diameter. The correction factors calculated by Kato (2005) were employed for matrix correction.

4. RESULTS

4.1. Mineral assemblages and microstructures of analyzed serpentinite samples from the Yuli belt

A total of 25 serpentinite samples were collected from the Yuli Belt and analyzed for this study. A representative selection of seven serpentinite samples with varying microstructures (Fig. 4) and mineral assemblages (Table 1) were chosen for more detailed analyses. All samples were mostly composed of antigorite along with an array of accessory minerals, such as magnetite, magnesite and talc. In addition, one sample was rich in metamorphic olivine. However, no remnant primary olivine or pyroxene was observed in the serpentinite samples. Also, although brucite has been identified from the Juisui serpentinites in previous studies (Dewangga, 2019), no brucite was observed in any of the samples analyzed for this study.

Samples selected from the Wanjung region contain carbonate mineral veins mostly consisting of magnesite (Fig 4a). They also contain clusters of magnetite, as well as some primary Cr-spinel. Accessory minerals include sulfide minerals, ankerite and pentlandite.

Three samples from the Mt. Tsunkuan serpentinite body in the Juisui region were chosen for more detailed analyses. Sample Ts9 is from the contact zone of the serpentinite body and the pelitic schist. In addition to antigorite, Ts9 contains magnetite, talc and some accessory pyrite. Microstructural observations show that during the formation of talc veins, new antigorite veins were also formed (Fig. 4b). The sample also contains bastite, a pseudomorph after pyroxene, which is a characteristic serpentinite microstructure in the Juisui region. Sample Ts12 is a typical sample from the Mt. Tsunkuan serpentinite body, which are mostly made up of platy or needle shaped antigorite, thin fibrous antigorite veins and some

minor magnetite. Sample Ts33 contains a large fibrous antigorite vein, which is several centimeters thick (Fig. 3c). The microstructures of the fibrous vein are complex and the antigorite grains are elongated rather than truly fibrous (Fig. 4c). The fibrous veins contain granular antigorite with unusually high relief and high interference colors (Fig. 4c). Overall, the interference colors of the antigorites are higher in the vein than in the matrix. The matrix of sample Ts33 is quite rich in magnetite, whereas no magnetite occurs in the vein.

Samples from the Chinshuichi serpentinite body are characterized by fine grained clusters of magnetite (Fig. 4d). Unlike other samples we collected from Yuli Belt, sample DK155 contains abundant metamorphic olivine (Fig 4e). The samples, such as sample DK157, collected from the talc rich contact zone of the serpentinite body and pelitic schist contain almost no magnetite. The microstructure of DK157 (Fig. 4f) is slightly sheared and contains patches of more iron oxide enriched antigorite, which could be interpreted as remnants of broken down magnetite.

4.2. ATR-IR spectra of antigorites

The ATR-IR spectrum of antigorite contains two main absorbance bands, the Si-O absorbance band and the O-H absorbance band (Fig. 5). These two absorbance bands correspond to the vibrations of the respective molecular bonds in the crystal structure of antigorite. The intensity and wavenumber of the absorbance of these main absorbance bands are affected by changes in the chemical composition and crystal structure of antigorite. There are also several smaller absorbance bands in the spectra of antigorite, which correspond to different vibrational modes of the Si-O and O-H bonds. In this study, we focus on looking at how different chemical compositions and microstructures affect the main Si-O and O-H absorbance bands.

Figure 6 shows the wavenumber values of the main Si-O and O-H absorbance bands of antigorites from the Juisui, Wanjung and Chinshuichi regions of the Yuli Belt. The results of

the ATR-IR measurements are overall quite scattered. However, more careful examination of the results reveal a few interesting trends. Firstly, the serpentinite samples in the Juisui region can be divided into two groups based on the wavenumber value of the O-H absorbance peak. O-H absorbance values of antigorites in samples Ts9 and Ts12 are between 3652-3663 cm^{-1}, whereas the O-H absorbance values measured from sample Ts33 are between 3665-3672 cm^{-1}. The O-H absorbance values of antigorites from the Wanjung and Chinshuichi regions fall between 3662-3669 cm^{-1}, which is between the values of the two Juisui region O-H absorbance groups. Secondly, The Si-O absorbance values of most measurements vary between 946-961 cm^{-1}. However, the Si-O absorbance values of antigorites measured from the large fibrous vein in sample Ts33 are roughly between 961-966 cm^{-1}, which is higher than Si-O absorbance values measured from the other samples.

4.3. The composition of antigorites

Representative chemical composition data of antigorites from each region is shown in Table 2. Out of all the elements, Fe and Mg had the most variation within the Yuli Belt antigorites (Fig. 7). The results can be divided into roughly three groups. The first group contains the high Fe (~4.7 pfu) and low Mg (~41 pfu) antigorites from samples Ts9, Ts12 from the Juisui region and sample DK157 from the Chinshuichi region. Samples Ts33 from the Juisui region and DK157 from the Chinshuichi region have a low Fe (~0.8 pfu) and high Mg content (~45.5 pfu) and form the second group. The third group is made up of measurement from the Wanjung samples and their Fe and Mg values plot on a continuous line between the two endmember groups.

Another pair of elements that had noticeable variation between all the samples was Al and Si (Fig. 8). However, in the case of Al and Si, the differences are not as large and there is more scattering within each sample. For example, antigorites measured from the matrix and

bastite in sample Ts9 have a higher Al content and lower Si content than antigorites measured from talc-rich veins in sample Ts9. Most of Ts33 measurements have a lower Al content (~0.8 pfu) and a higher Si content (~33.9 pfu) than samples Ts9 and Ts12 from the same serpentinite body, with respective values of ~1.7 pfu and 33.6 pfu. This time the Wanjung samples, W090617 and W090623, plot closer to measurements made from Ts33 whereas measurements from the Chinshuichi samples, DK155 and DK157, plot in between the two endmember groups.

5. DISCUSSION

5.1. Metamorphic history of Yuli Belt serpentinites

Since serpentinites lack minerals suitable for detailed geothermobarometry, it can be challenging to constrain the metamorphic history of the serpentinites. The task is made even harder by the widespread fluid mediated Barrovian-type greenschist-facies metamorphic overprinting (e.g. Liou, 1981; Lo and Yui, 1996; Yui et al., 2014), which seems to have eradicated most of the metamorphic index minerals from the metasediments in the Yuli Belt. However, recent studies (Chih-Ying, 2019; Kouketsu et al., 2019) on peak metamorphic temperatures of pelitic schists in the Yuli Belt, made using the Raman spectroscopy of carbonaceous material (RSCM) geothermometry method, reveal a wider distribution of peak metamorphic temperatures ranging from 340-620 °C in the different regions of Yuli Belt. Interestingly, Chih-Ying (2019) observed that RSCM analyses made from graphite-bearing quartz-mica schist samples that were collected from the vicinity of Yuli Belt serpentinite bodies yielded higher metamorphic temperatures, in the order of ~550-620 °C. This temperature range is on the upper end of antigorite stability (Evans, 2004) and fits well with the notion that no low-temperature serpentinite minerals such as lizardite and chrysotile were observed in the samples we studied. Although it is not completely clear at which point the serpentinite bodies were emplaced in the surrounding pelitic schists, the progressively increasing metamorphic

temperatures observed around the Yuli region serpentinite bodies suggest that the serpentinite bodies might have been buoyantly uplifted through the exhumation channel, in a process known as doming, due to the lower density of the serpentinites relative to the surrounding rocks. If this is the case, the metamorphic temperatures and pressures measured from the surrounding metasediments can serve as the minimum metamorphic conditions for the serpentinites. The rare occurrence of metamorphic olivine at the Chinshuichi serpentinite body would suggest that metamorphic temperatures reached an excess 640 °C around the Chinshuichi serpentinite bodies. Since the serpentinites seem to have experienced metamorphic temperatures close to those obtained from the surrounding metasediments using RSCM thermometry, it is likely that the serpentinites and metasedimentary rocks were mostly metamorphosed isofacially, as was proposed by Dewangga (2019).

5.2. Compositional and microstructural variation of Yuli Belt serpentinites

There were clear differences in antigorite microstructure and composition between samples collected from a single serpentinite body, indicating several pulses of subduction zone fluid flow. For example, the Si content of recrystallized antigorite was higher in the talc rich veins than in matrix antigorites in sample Ts9 (Fig. 8). The talc veins and the Si-rich antigorites were formed by a Si-rich fluid, which flowed through the contact zone of the pelitic schist and the Mt. Tsunkuan serpentinite body. The linear change of Si and Al content in sample Ts9 antigorites suggest that Si is replacing Al in the antigorite structure. Curiously, this replacement is not reflected in a similarly linear way in the ATR-IR spectrum of antigorite (Fig. 6), despite the fact that there is quite a large difference in the 4-fold coordination ionic radii of Si^{4+} and Al^{3+}, which are 0.34 Å and 0.47 Å, respectively (Whittaker and Muntus, 1970). This observation is in line with a Raman study on antigorite structure by Kouketsu et al. (in review), which also noted that variations in Si and Al content did not have a clear correlation with the

Raman spectrum Si-O absorbance peaks of antigorite. Based on these observations, it would appear that the vibrational energy absorbed by the Si-O and the Al-O bonds are quite similar.

There was, however, significant variation in the wavenumber value of the main Si-O absorbance band with values ranging between 946-970 cm^{-1}. Despite careful comparisons between all different elements (listed in Table 2) measured from the antigorites, no clear connection between any element and the Si-O absorbance peak values could be established. However, there was a clear difference between the Si-O absorbance value of the Ts33 veins and the matrix. The ATR-IR measurements made from the large fibrous vein had higher values (~961-966 cm^{-1}) than the measurements made from the matrix (~949-961 cm^{-1}). Since antigorite compositions in the matrix and veins are very similar, the difference in the wavenumber value of the Si-O absorbance peak must be due to differences in the crystal structure. This is supported by the observation of granular antigorite microstructures, with unusually high relief and high interference colors, in sample Ts33 (Fig. 4c) that suggest that the crystal structure of antigorites has been deformed. It is possible that the deformation of the antigorite crystal structure could be an early sign in antigorite breakdown. However, despite carefully measuring ATR-IR spectrum of fibrous antigorites from several locations, we could not confirm the presence of metamorphic olivine.

One possibility is that the m-values of vein antigorites were altered during the vein formation. Several studies (Padrón-Navarta et al., 2008; Wunder et al., 2001) have suggested that the shortening of the m-value might be related to increasing metamorphic temperatures. However, the results have not been consistent (Auzende et al., 2006; Mellini et al., 1987), and it has been argued that processes, such as shearing, can also cause variation in the m-values of antigorite. It is also possible that the kinetically rapid growth of the fibrous vein antigorites caused the formation of structural defects. For example, a TEM study by Dódony and Buseck (2004) revealed that the periodically reversing wave-like structure of antigorite tends to often

be asymmetrical and sometimes mixed with curled up chrysotile fibers. A detailed TEM investigation of the fibrous antigorite vein in sample Ts33 would be necessary to find out what is causing the unusually high wavenumber values of Si-O bonds.

The Mg and Fe values in Figure 7 follow a linear trendline suggesting an almost 1:1 replacement of Mg by Fe. This result is reflected in the O-H absorbance values of antigorite (Fig. 6), where samples with high Fe content (~4.8 pfu) plot between 3652-3663 cm^{-1} and samples with low Fe content (~0.8 pfu) plot between 3665-3672 cm^{-1}. These results are in agreement with previous studies (Mellini et al., 2002; Sakaguchi et al., 2020) that suggest the octahedral replacement of Mg by Fe will result in lower O-H wavenumber. Interestingly the compositions of the vein antigorites do not differ from the matrix antigorites in sample Ts33. It might be that fluids that created the vein circulated along grain boundaries and altered the composition of the surrounding matrix as well. It is also possible that the variation in Fe content might reflect variations that were already present in the protolith during primary serpentinization. However, since variation in the Fe content is so large, it is more plausible that it is caused by the inflow of metasomatic fluids that penetrated the serpentinite body and spread around along grain boundaries.

We were also interested to see if the ATR-IR spectra of antigorites in sample DK155, which is the only sample that contains metamorphic olivine, would have any features that could be linked to the dehydration of antigorite. However, no structurally distinct features were observed in the ATR-IR spectra of antigorites in sample DK155 (Fig. 6). DK155 does plot together with sample Ts33 in the Mg vs. Fe diagram (Fig. 7), which doesn't contain olivine but contains microstructures that could be interpreted as early signs of antigorite breakdown. Could it be that the dehydration of antigorite depletes it of Fe? According to several studies (e.g. (Bretscher et al., 2018; Merkulova et al., 2016; Padrón-Navarta et al., 2011) it seems that the opposite is true. For example, Padron-Navarta et al. (2011) studied the compositional variation

in a single serpentine body with a continuous antigorite dehydration front from pure Atg-serpentinite to Chl-harzburgite and they observed that the Mg# of antigorite decreases and the Mg# of Ol increases with progressive metamorphism. Also, the difference in total Fe composition of Atg-serpentinite and dehydration zone antigorites was much smaller (<1.5 wt%) in the study by Padron-Navarta et al. (2011) than in our study (>6.5 wt%).

5.3. Nature of metasomatism in the Yuli Belt serpentinites

These large and somewhat inconsistent variations in antigorite composition in the Yuli Belt serpentinites highlight the heterogeneous nature of the metasomatic fluids in the subduction zone. Recently, researchers have become increasingly interested in Fe mobility during subduction (Debret et al., 2016) as well as the role Fe plays in controlling the oxidation state of subduction zone fluids (Debret et al., 2015, 2014). Microstructural observations of magnetite breakdown in the contact zone sample from Chinshuichi area point to the mobilization of Fe. The other serpentinite samples collected from the Chinshuichi region contain large magnetite clusters (Fig. 4d), whereas sample DK157 contains virtually no magnetite, just weak iron-oxide stained pseudomorphs of the original magnetite (Fig. 4f). Fe is not a particularly easily mobilized element but it can be mobilized by Fe(II)-Cl and/or Fe(II)-(HS) in reduced fluids (Chen et al., 2019) or by Fe(II)-SO_X or Fe(II)-Cl_2 (Debret et al., 2016) or Fe(II)-CO_3 (Debret et al., 2018) in oxidized fluids. The magnesite veins (Figs. 3d) and the various sulfide minerals (Table 1) observed in the Chinshuichi region provide evidence that the fluids that penetrated the serpentinite body contained SO_X or HS^- and CO_X species necessary to mobilize Fe. However, it is difficult to say whether the fluid in the subduction zone was reduced or oxidized since both SO_X and HS^- can mobilize Fe. Carbonin et al., (2015), who studied rodingite bearing serpentinites with very high degrees of magnetite, similar to those observed in the Wanjung

and Chinshuichi regions, found that large clusters of magnetite with associated Fe-Ni sulfides were formed when the serpentinites experienced strong metasomatism by CO_2-rich fluids.

Furthermore, the different alteration zones and veins observed in and around the serpentinites show that the serpentinites were metasomatized by fluids with varying compositions. For example, talc rich contact zones are a typical feature of serpentinites and they are formed by Si-rich fluids, which usually originate from surrounding sedimentary rocks (Manning, 2004) whereas magnesite veins are formed by CO_2-rich fluids. Chlorite and amphibole rich shear zones are also a typical feature of ophiolitic serpentinites in oceanic settings and Boschi et al., (2006) argued that they are formed by Si-Al-Ca rich metasomatic fluids emanating from gabbroic rocks and serpentinites. Rodingites, observed in the Chinshuichi region, are also characteristics of serpentinites that are in contact with Ca-bearing CO_2-rich fluids that are produced by the metasomatism of gabbroic rocks (Bach and Klein, 2009). There is no clear consensus on how the albite-rich rocks observed around the Yuli Belt serpentinites were formed but they might be connected to the sodic metasomatism in the subduction zone. Keyser et al. (2016) suggested that the protolith might be meta-plagiogranite but Lo et al., (2020) have also proposed that the protolith of the albite-rich rocks might be altered gabbro or jadeitite formed by sodic metasomatism. While none of the serpentinite bodies we studied were a part of a clear ophiolite sequence, metasomatic interactions with the surrounding metagabbroes seem to account for many of the metasomatic alteration zones observed around the Yuli Belt serpentinites. Baziotis et al. (2017) suggest that the conditions during peak metamorphism were relatively dry and that limited fluid flow occurred mainly along grain boundaries. It has been proposed by Yui et al. (2014) that the collision of the Luzon arc to the Chinese continental margin, which resulted in the rapid uplift of the Yuli Belt, might have also induced increased fluid flow in the subduction zone. Exhumation related fluid flow

would also account for the widespread greenschist-facies metamorphic overprinting observed in the Yuli Belt.

6. CONCLUSIONS

The varying antigorite compositions and the abundance of various metasomatic veins and alteration zones in and around the Yuli Belt serpentinite bodies point to active fluid flow in the subduction zone. The majority of fluid flow in the serpentinites we studied seems to have been focused on the sheared contact zone of the serpentinites and the surrounding metasediments with occasional events of vein forming fluid flow that penetrated to the deeper parts of the serpentinite bodies.

While some systematic variations in the ATR-IR spectrum of antigorite could be observed, such as the effect of Fe content on the wavenumber value of the O-H absorbance band, no conclusive observations of changes in the crystal structure of antigorite, which could be linked to the varying metamorphic conditions of Yuli belt, were found. The overall ATR-IR results are rather scattered and probably influenced by naturally occurring random variation in the antigorite crystal structure. Also, since the ATR-IR spectrum is affected by both the chemical composition and the crystal structure of antigorite it is often difficult to distinguish the effect of one from the other without detailed TEM observations.

Many open questions still remain about the nature of metasomatism and the complex metasomatic interactions between the different lithologies in the Yuli Belt. However, it seems clear that the serpentinites, as well as the other mafic rocks in the Yuli Belt, seem to have had a large impact on the composition of the metasomatic fluid in the subduction zone. Further studies on redox sensitive elements, such as C, S and Fe, as well as more detailed analyses of magnetite the various sulfide minerals in the serpentinites might help us understand the redox conditions of the metasomatic fluids in the Yuli Belt during subduction/exhumation.
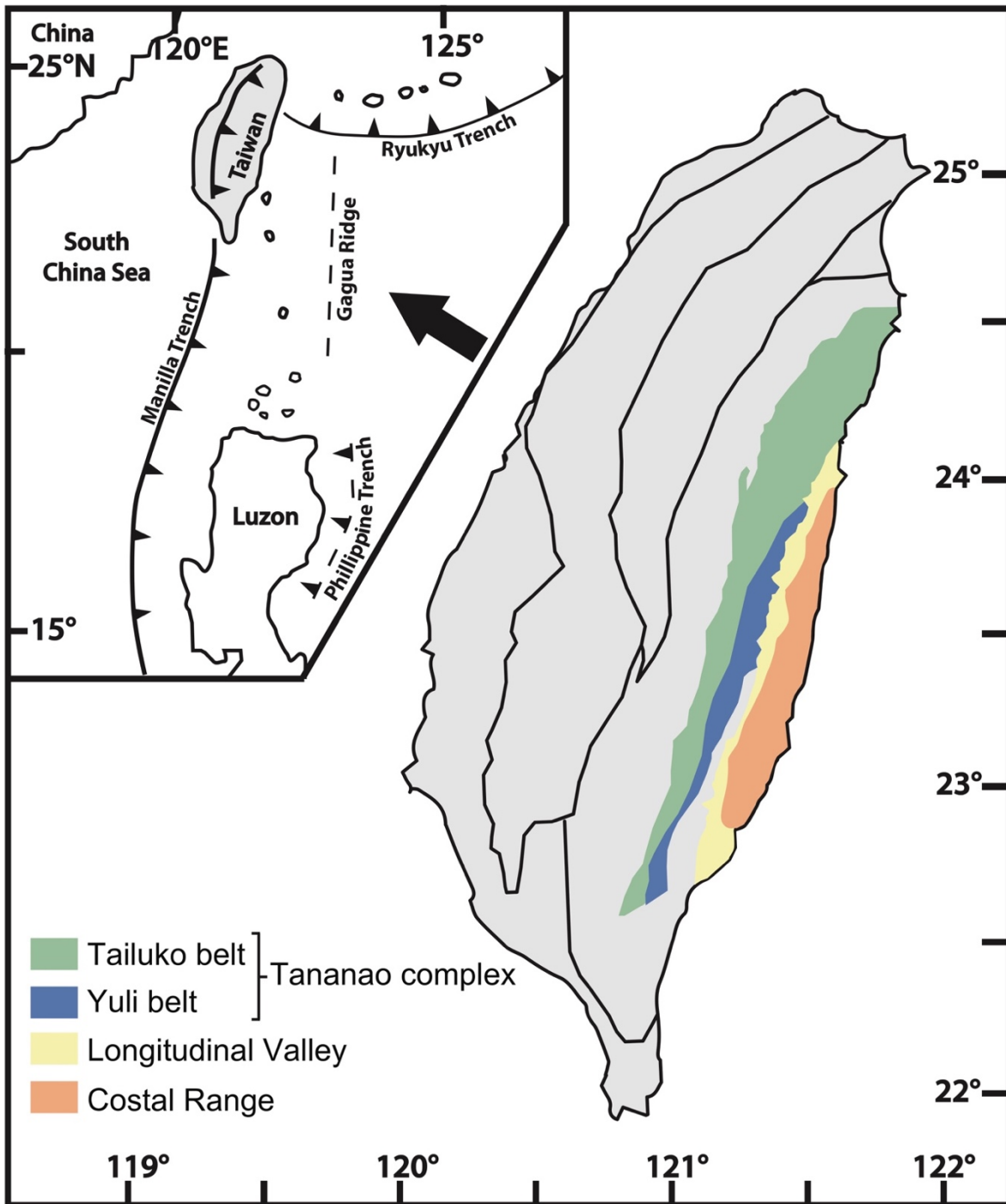
Figure 1. The tectonic setting of Taiwan and a simplified geological map of Taiwan showing the locations of the Tananao complex, the Longitudinal Valley and the Costal Range (Modified after Kouketsu et al., 2019; Yui et al., 2014).
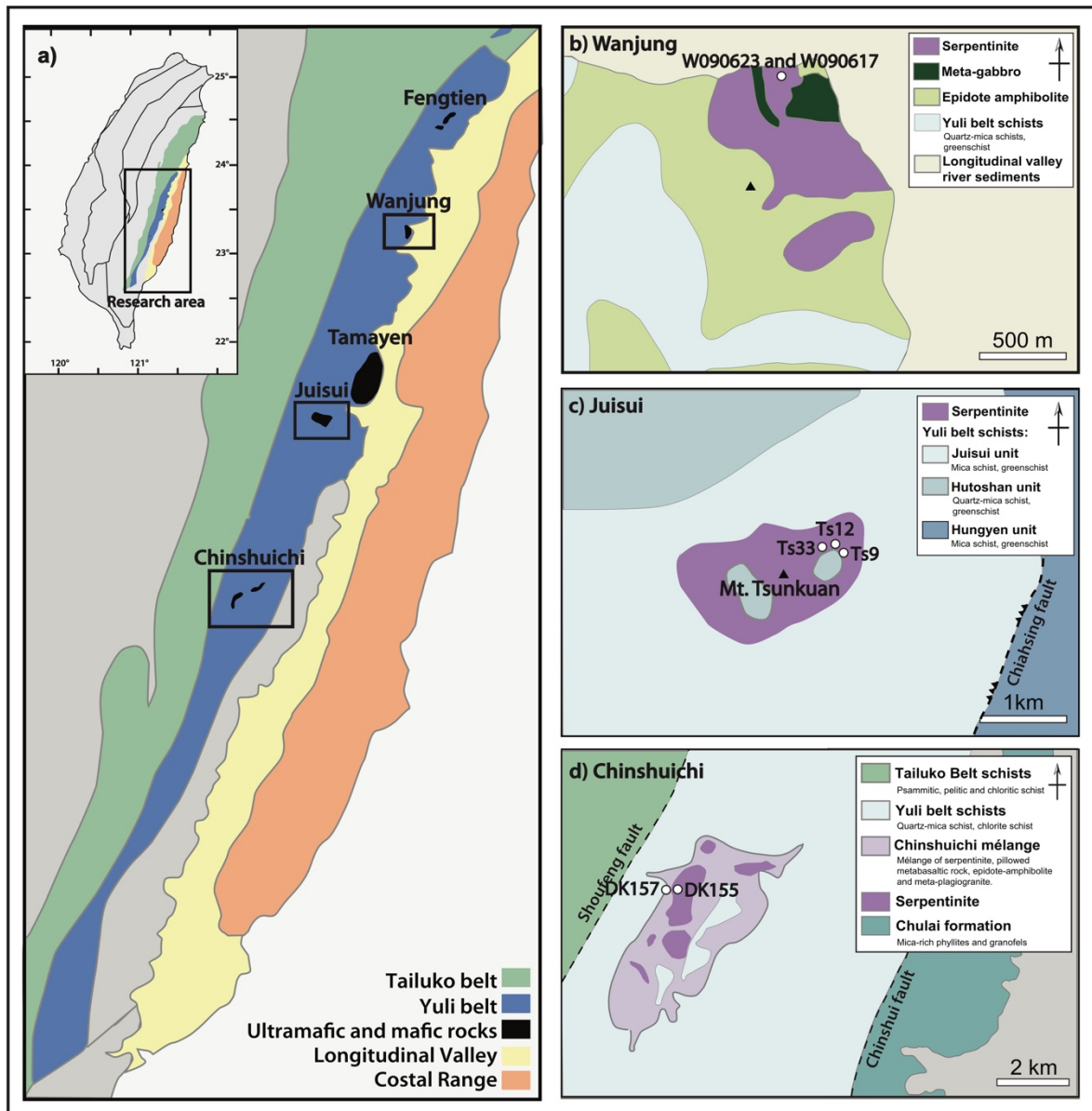
Figure 2. a) Simplified geological map of the Yuli belt and the serpentinites bodies in the b) Wanjung, c) Juisui, and d) Chinshuichi regions (Modified after Chen et al., 2000; Dewangga, 2019; Keyser et al., 2016 and Lan, 2011). Sampling locations of the samples described in this study are also indicated.
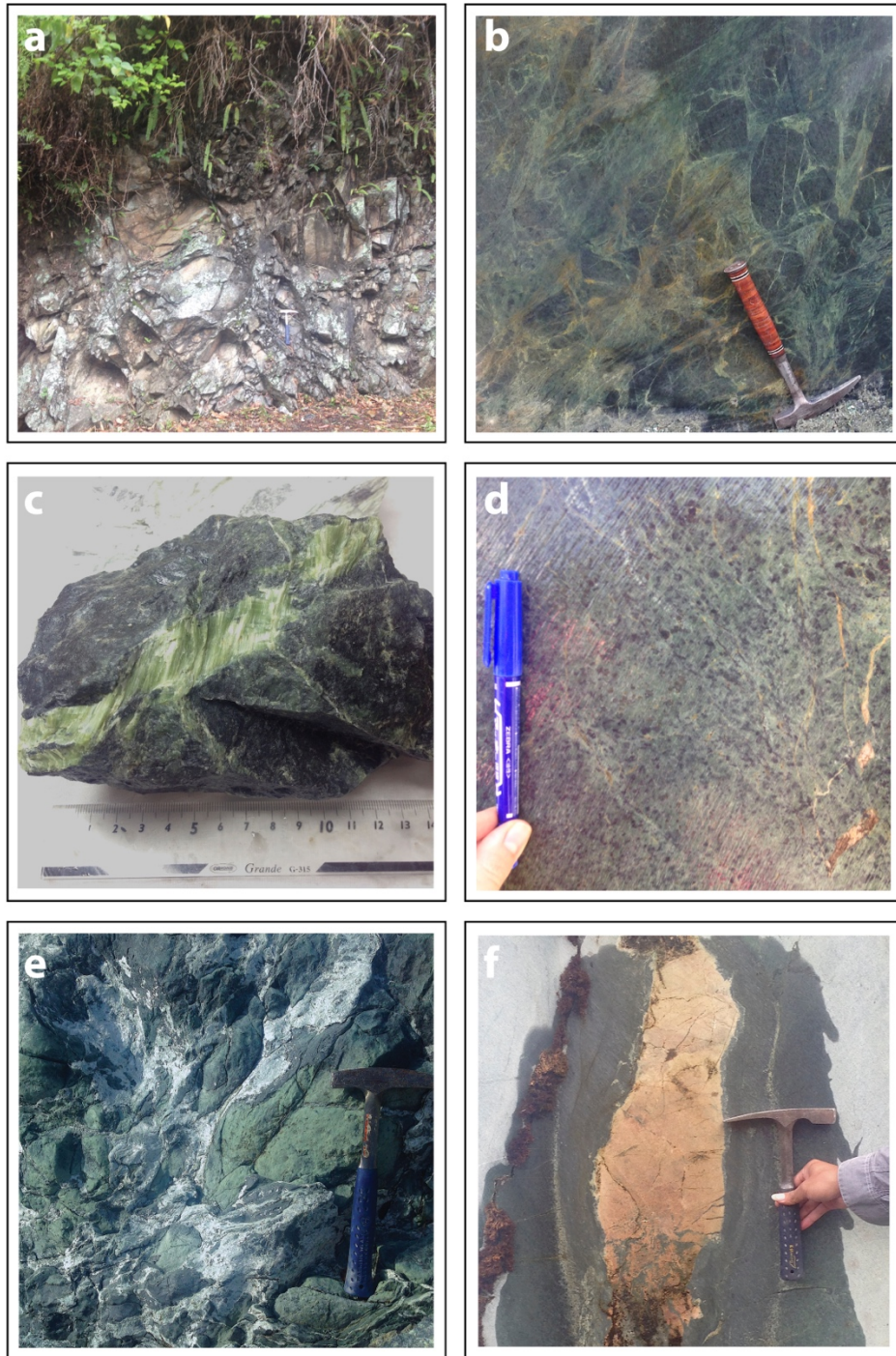
Figure 3. Mesoscopic structures of metaserpentinites in the Yuli belt. Hammers used as a scale are approximately 30 cm long a) Weathered outcrop mostly covered by undergrowth in the Wanjung region. b) Brecciated serpentinite at Mt. Tsunkuan quarry. c) Large fibrous antigorite vein in sample Ts33 collected from the Mt. Tsunkuan quarry. d) Mesoscopic magnetite clusters and thin carbonate mineral veins in serpentinite in the Chinshuichi region. e) Sheared, talc and rich contact zone of pelitic schist and serpentinite in the Chinshuichi region. f) A thick garnet-rich rodingite vein running through serpentinite in the Chinshuichi region.
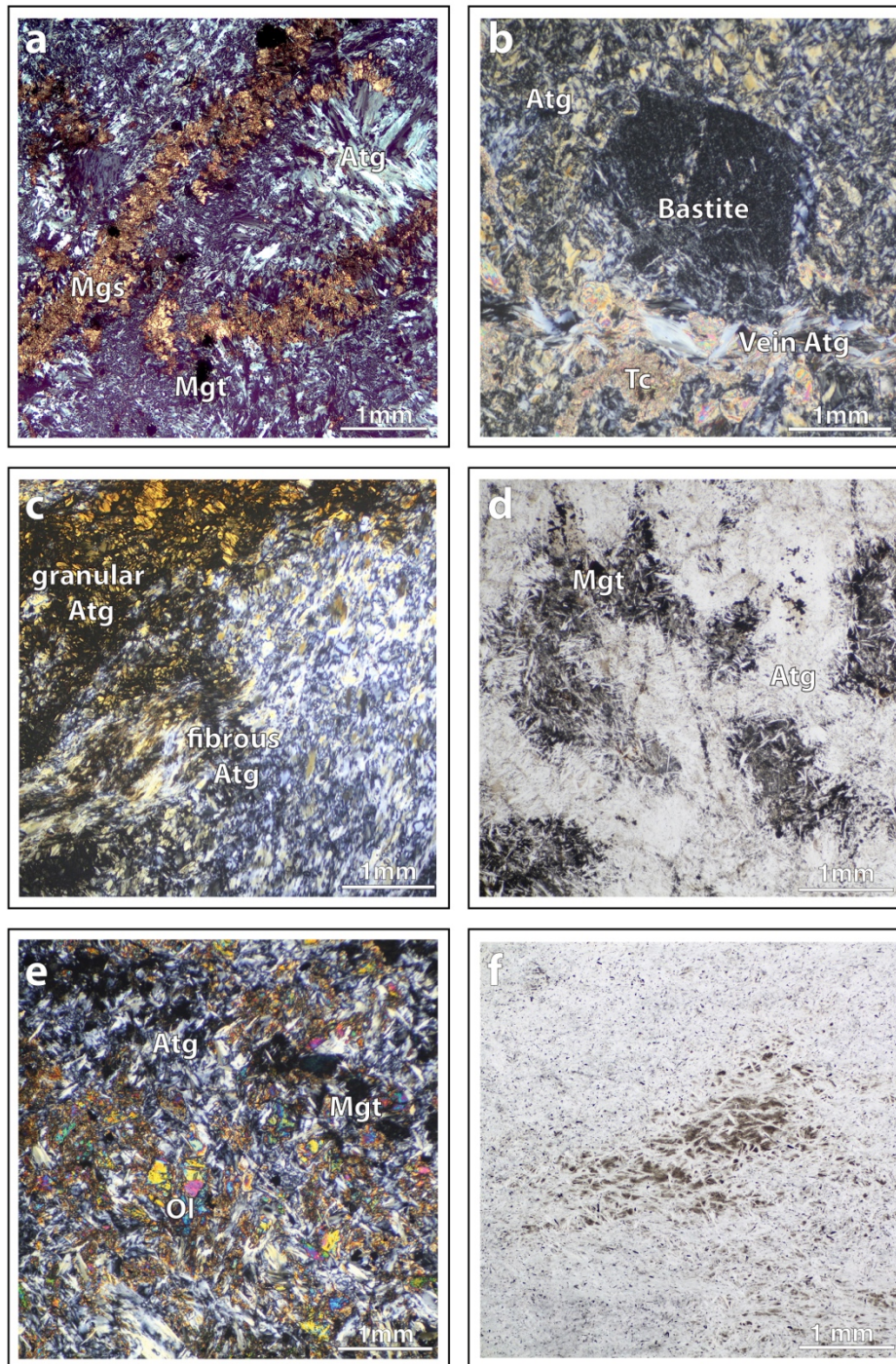
Figure 4. Photomicrographs of samples analyzed for this study. Atg, antigorite; Mgs, magnesite; Mgt, magnetite; Ol, olivine; Tc, talc. a) Antigorite and magnesite in sample W09617. b) Talc veins and recrystallized vein antigorite in antigorite matrix in sample Ts9. c) High relief antigorite with unusually high interference color and elongated antigorite crystals in fibrous antigorite vein in sample Ts33. d) Large clusters of magnetite in an antigorite matrix in sample DK152. e) Metamorphic olivine in a matrix of antigorite and magnetite in sample DK155. f) Pseudomorphic microstructure in an sheared antigorite-only sample, DK157.
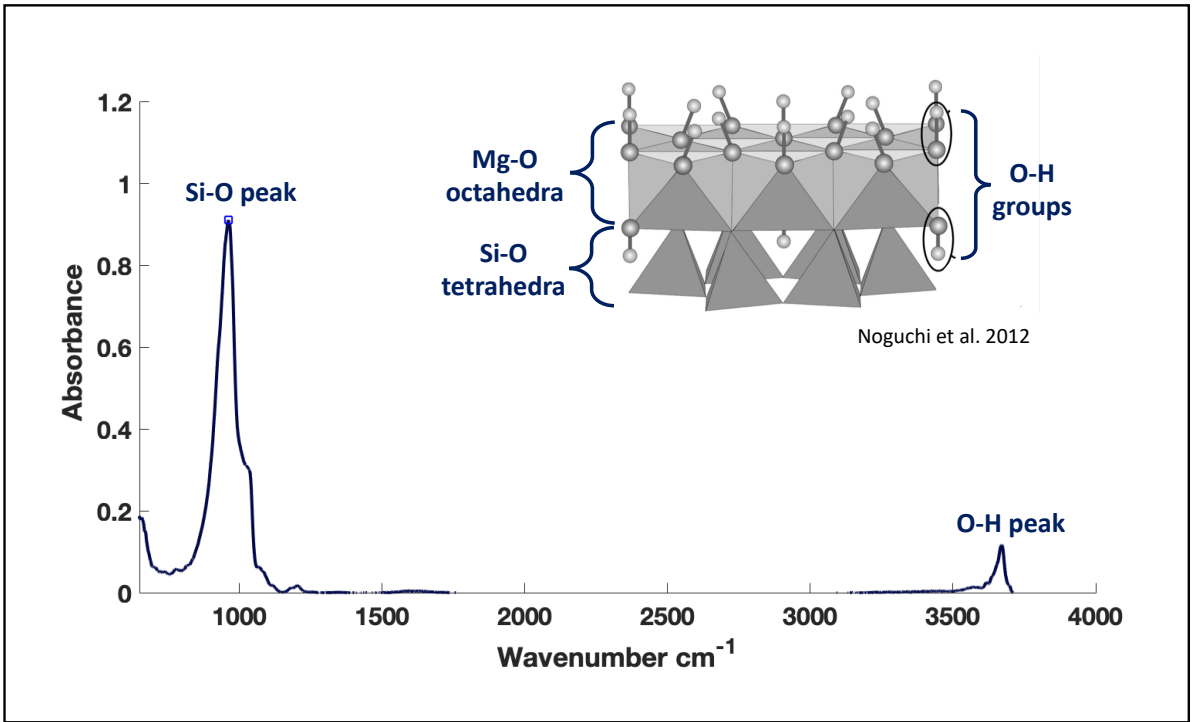
Figure 5. The Si-O and O-H absorbance peaks in the ATR-IR spectra of antigorite and the basic crystal structure of antigorite (Modified after Noguchi et al. 2012).
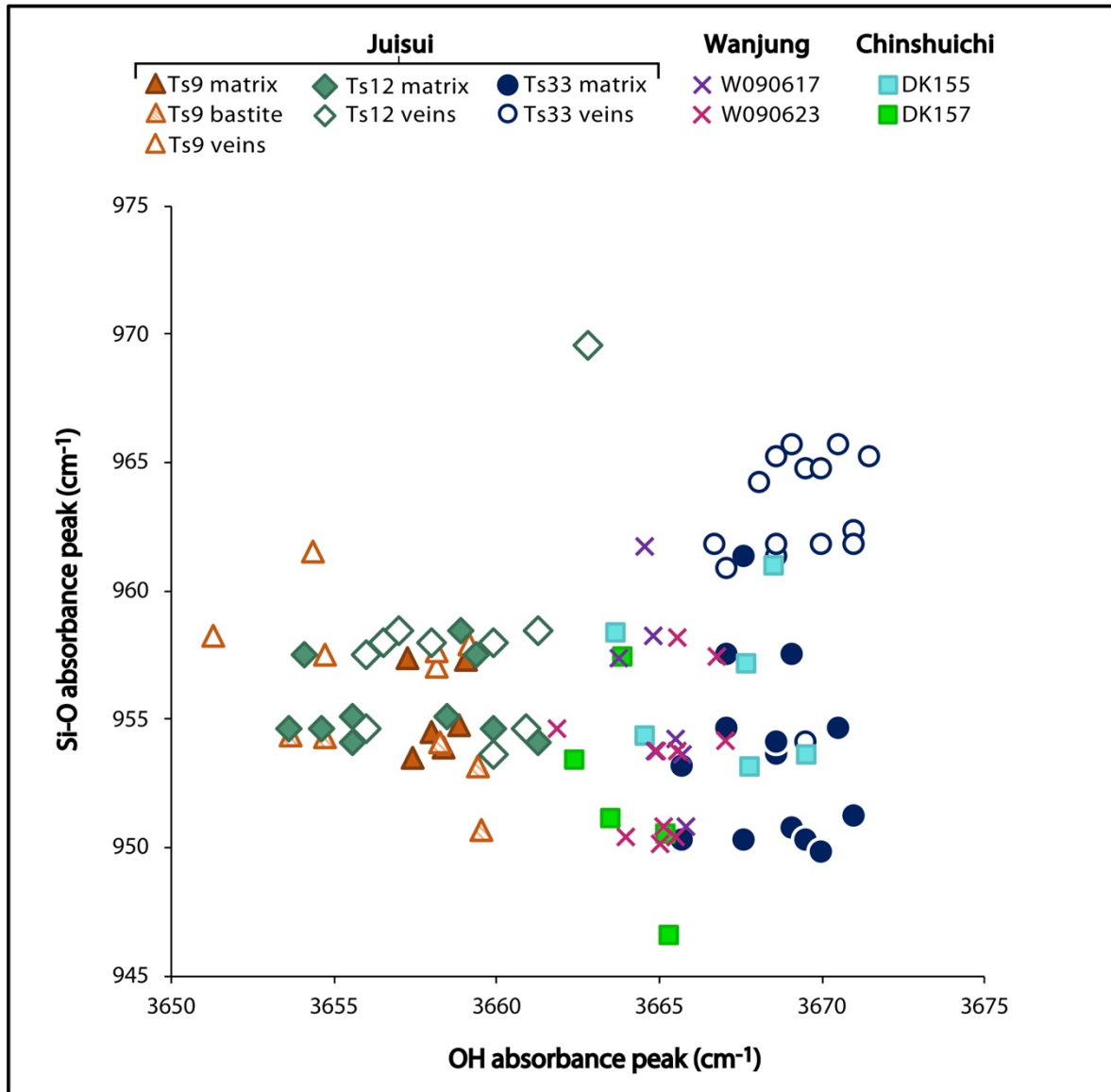
Figure 6. Si-O and O-H absorbance peak values in the ATR-IR spectra of antigorites from serpentinites in the Juisui, Wanjung and Chinshuichi regions of the Yuli Belt.
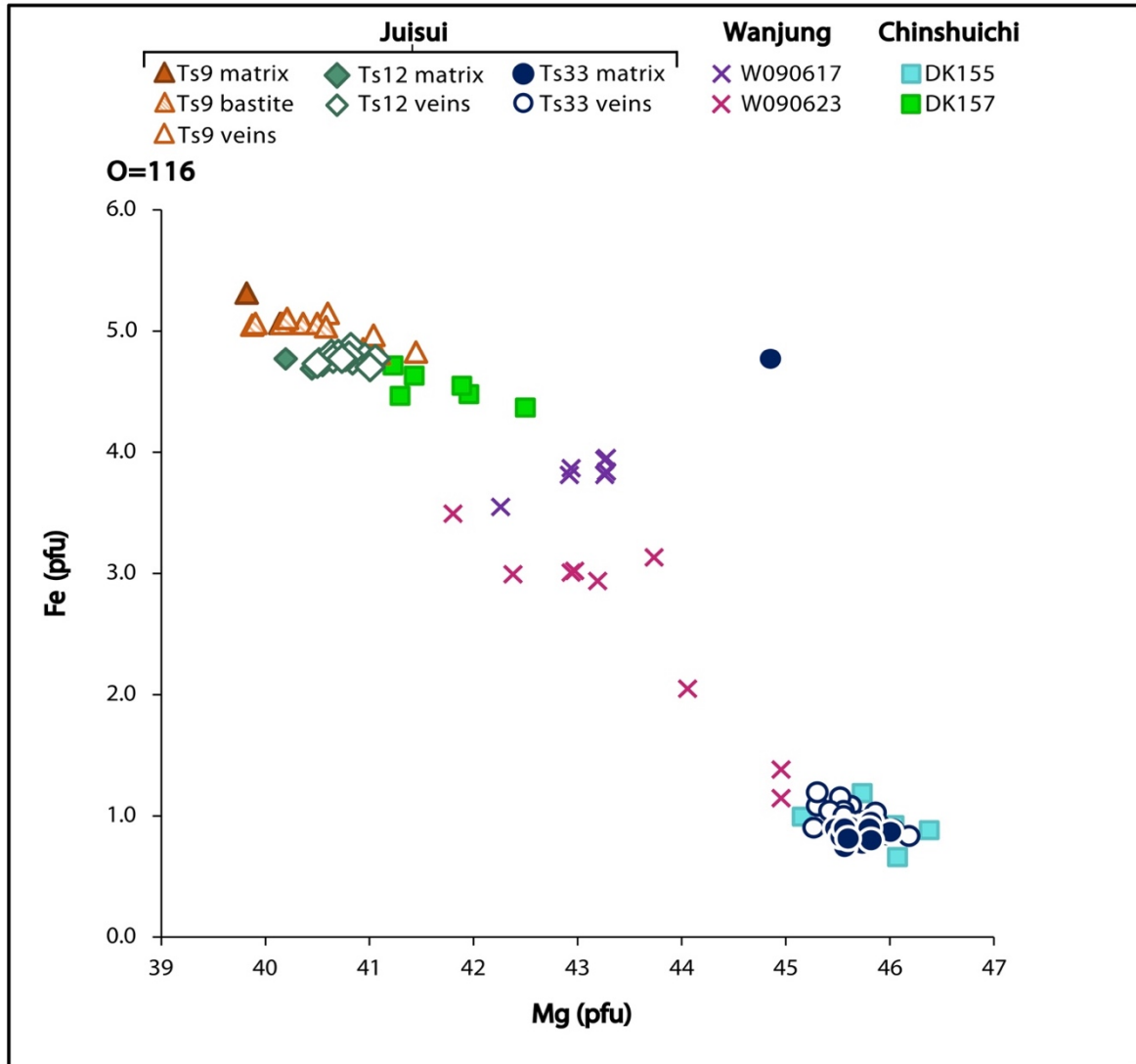
Figure 7. Fe and Mg concentration of antigorites from serpentinites in the Juisui, Wanjung and Chinshuichi regions of the Yuli Belt. The results are shown per formula unit (pfu) as calculated for 116 O.

Figure 8. Al and Si concentration of antigorites from serpentinites in the Juisui, Wanjung and Chinshuichi regions of the Yuli Belt. The results are shown per formula unit (pfu) as calculated for 116 O.
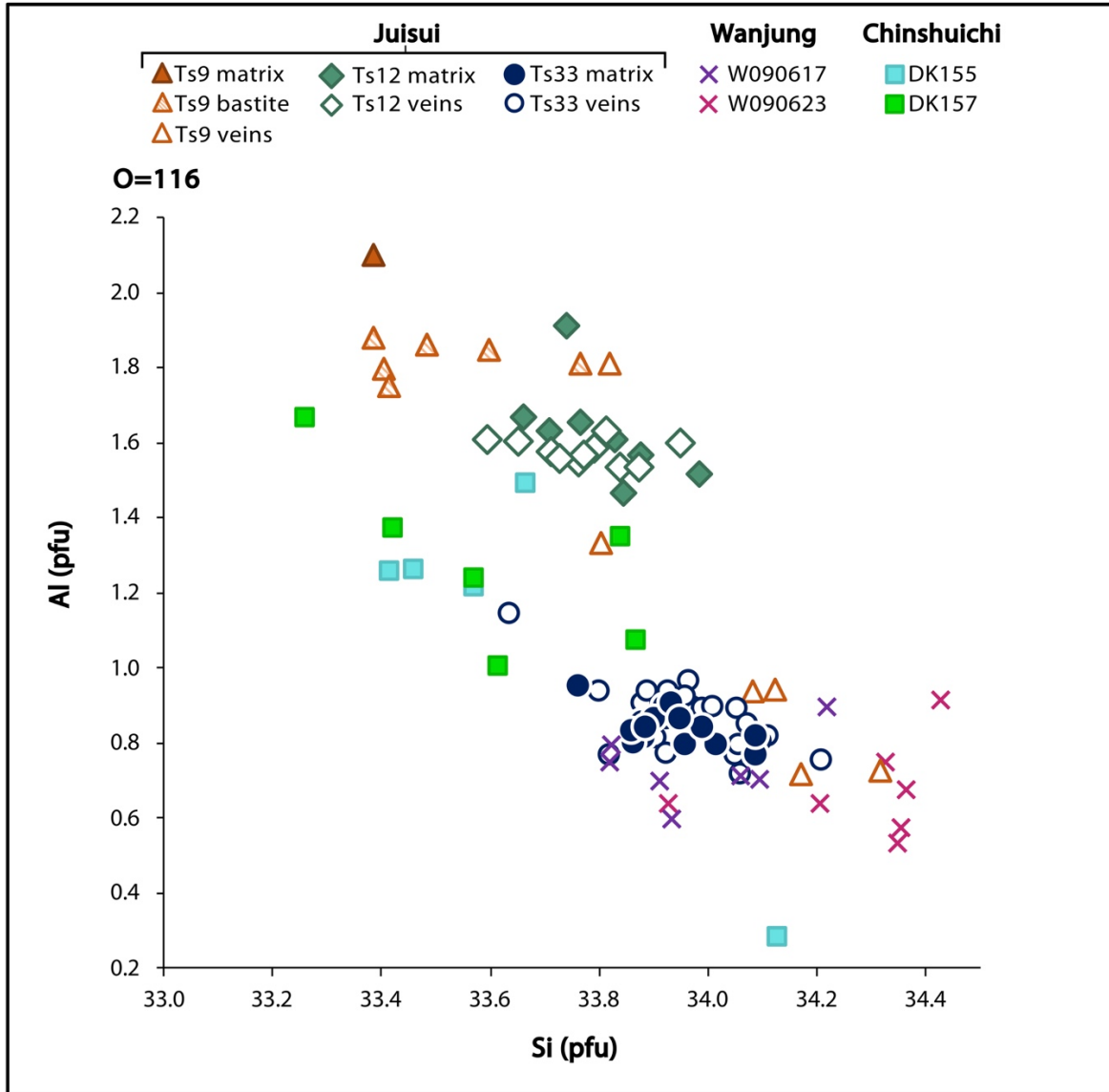
Table 1. Mineral assemblages of analyzed serpentinite samples from the Wanjung, Juisui and Chinshuichi regions of the Yuli Belt.

Sample No.	Atg	Ol	Mgt	Cr-Spl	Mgs	Dol	Tlc	Py	Ank	Pn
Wanjung										
W090617	++		+	-	+	-			-	-
W090623	++		+	-	+	-				
Juisui										
Ts9	++		-				+	-		
Ts12	++		-	-						
Ts33	++		+	-						
Chinshuichi										
DK155	++	++	+	-				-		-
DK157	++									

Table 2. Representative antigorite compositions from Yuli belt serpentinite samples. Total iron is shown as FeO and Mg# = (Mg/(Mg + Fe)).

Sampling area	Wanjung		Juisui			Chinshuichi	
Sample	W090617	W090623	Ts9	Ts12	Ts33	DK155	DK157
SiO$_2$ wt%	42.49	43.68	43.05	42.66	43.20	43.90	42.43
TiO$_2$	0.00	0.04	0.04	0.00	0.00	0.00	0.00
Al$_2$O$_3$	0.75	0.69	1.44	1.70	0.83	1.36	1.48
Cr$_2$O$_3$	0.00	0.14	0.34	0.24	0.06	0.34	0.41
FeO	5.68	4.48	7.84	7.36	1.27	1.58	6.80
NiO	0.02	0.43	0.27	0.28	0.19	0.03	0.27
MnO	0.00	0.05	0.17	0.16	0.02	0.04	0.14
MgO	35.89	37.01	34.70	34.66	39.58	39.95	35.73
CaO	0.00	0.02	0.00	0.01	0.00	0.00	0.01
Na$_2$O	0.01	0.00	0.00	0.01	0.00	0.00	0.01
K$_2$O	0.00	0.01	0.01	0.01	0.00	0.00	0.01
Total	84.85	86.59	87.86	87.10	85.16	87.21	87.28
Numbers of ions on the basis of O = 116							
Si	34.09	34.20	33.80	33.71	33.82	33.60	33.42
Ti	0.00	0.02	0.02	0.00	0.00	0.00	0.00
Al	0.71	0.64	1.34	1.58	0.77	1.23	1.38
Cr	0.00	0.08	0.21	0.15	0.03	0.21	0.25
Fe	3.81	2.94	5.15	4.86	0.83	1.01	4.48
Ni	0.01	0.27	0.17	0.18	0.12	0.02	0.17
Mn	0.00	0.00	0.00	0.00	0.00	0.00	0.00
Mg	42.92	43.20	40.60	40.83	46.19	45.59	41.96
Ca	0.00	0.01	0.00	0.01	0.00	0.00	0.01
Na	0.00	0.00	0.00	0.01	0.00	0.00	0.00
K	0.00	0.01	0.01	0.00	0.00	0.00	0.01
Sum cation	81.55	81.38	81.29	81.32	81.77	81.65	81.67
Mg#	0.918	0.936	0.888	0.894	0.982	0.978	0.904

Part 3:

Quantitative approach to the study of vibrational spectroscopy data

ABSTRACT

A new data processing algorithm was developed to tackle the problem of processing large spectral datasets of attenuated total reflection infrared spectroscopy (ATR-IR) mapping data. The algorithm outlined in this chapter is divided into two sections. The first algorithm makes it possible to determine the wavenumber value and absorbance intensity of the highest intensity absorbance peak within a certain spectral range from a large number of mapping spectra. The second algorithm can be used to reconstruct the spectral map using the processed data. The algorithm was specifically developed to analyze the ATR-IR data measured from serpentinite samples but it can be used to process a variety of spectral data. Recent advances in the application of vibrational spectroscopy methods, Raman spectroscopy and infrared spectroscopy, require increasing amounts of complex data processing and therefore further development of the algorithm outlined in this chapter could open new research avenues in the field of mineral spectroscopy.

1. INTRODUCTION

Vibrational spectroscopy methods, Raman spectroscopy and infrared spectroscopy, are standard mineralogical methods used to identify different mineral species. These methods are based on observing different vibrational modes of molecular bonds and functional groups. The vibration of each molecular bond in the crystal structure of a mineral absorbs a specific amount of energy, which can be recorded by a spectrometer. Hence, observing the Raman and infrared spectra of a specific mineral is a straightforward way of identifying a mineral. However, in the past twenty years the field of mineral spectroscopy has been rapidly evolving and more advanced mineralogical applications of vibrational spectroscopy have been introduced. For

example, various different mineral geothermobarometry methods that are based on Raman spectroscopy (e.g. Beyssac et al., 2002; Kohn, 2014) have been developed recently. In addition, several methods based on infrared spectroscopy have been developed to determine water content in rock and mineral samples (e.g. Lowenstern and Pitcher, 2013; Milliken and Mustard, 2005). These methods are dependent on observing slight differences in the peak intensities and absorbance wavenumber values of measured spectra and they demand more sophisticated methods of data processing, especially in the case of large mapping datasets.

A new quantitative method, which can be applied to analyze and visualize large spectral datasets, was developed as part of our research on the attenuated total reflection infrared spectroscopy (ATR-IR) of serpentinite minerals. The algorithm developed for this research can be used to calculate the peak positions and intensities of various types of spectral data, including Raman spectra and infrared spectra. The script for this algorithm is written in MATLAB but similar functions are also found in most other commercial data processing software. The following outline of the method gives a detailed explanation of the different parts of the algorithm and the subsequent discussion describes how this method could be applied in the field of mineral spectroscopy. The algorithm was especially developed to process spectral mapping data and thus the following explanation will be divided into two parts, the first part outlining how to determine the highest intensity absorbance peak in a certain wavenumber range and the second part explaining how to reconstruct the processed data back to a spectral map. The full scripts of the two algorithms are also attached in Appendix 1 and 2.

2. ANALYZED SAMPLE

The spectral data used to illustrate how the algorithm works is from an ATR-IR map of sample Ts33, an antigorite serpentinite sample collected from Mt. Tsunkuan serpentinite body in the Yuli belt, eastern Taiwan. The mapping area is located in between a fibrous antigorite vein and

a platy antigorite matrix, which also contains some magnetite (Fig. 1). This sample was chosen as an example, due to the large difference in the wavenumber values of the Si-O absorbance peaks of vein antigorite and matrix antigorite. The structure and composition of antigorites in sample Ts33 is discussed in detail in chapter 2 of this thesis.

3. OUTLINE OF THE ALGORITHM

3.1. Determining the highest intensity absorbance peak in a certain wavenumber range

To start the data processing, the spectral data needs to be exported from the spectrometer in a tabular data format, generally as a comma-separated values (CSV) file. Once the spectral data has been imported to the data processing computer, let the program know how to access the files by typing the following command into the command window:

```
sample='Ts33';

D = dir([sample,'_spectral_data/','data*']);
```

In this example, all the data that the program needs to access is in folder Ts33. For the algorithm to work properly, it is important that the MATLAB script is also saved in folder Ts33. The list folder contents (dir) command tells the program that the spectral data (D) that needs to be analyzed is in the spectral_data/ directory within the Ts33 folder and that each data point in the spectral data folder is followed by a running numbering (*), i.e. data1, data2, data3 etc.

Next, it should be specified that the array size should contain the whole dataset (D) and that the target variables determined by this algorithm are wavenumber values (xpks) and absorbance intensities (ypks) of the highest intensity absorbance peaks in the analyzed spectra:

```
n=size(D,1);

xpks=[],ypks=[]
```

Before letting the program analyze the data, it needs to be specified that when creating the first figure, the analyzed spectra should be also included in the figure:

```
figure ('Position', [400 700 1000 500]);

hold on
```

Using the 'hold on' function will allow the program to hold on to the analyzed data and add it all to one figure instead of creating individual plots of every spectra or every variable. The size and dimensions of the first figure are specified using the 'Position' function.

The fourth step is to define which part of the dataset the program should analyze and what function should be used to analyze the data. For each iteration (i), it is possible to decide, which section in the spectrum should be analyzed and how many spectra should be analyzed out of the whole dataset (e.g. every 100th spectrum (i = 1 : 100 : n). For the purpose of visualizing mapping data, it is necessary to analyze the whole dataset (i = 1 : n). For this iteration, the program needs to analyze .CSV data (csvread) located in the Ts33_spectral_data folder:

```
for i = 1:n

% Data for analysis

    filename=D(i).name

    IR_data=csvread([sample,'_spectral_data/',filename]);
```

The program also needs to be told that the x and y values are in the 1st and 2nd columns of each .CSV file:

```
% Set source for x and y values

    x=IR_data(:,1);

    y=IR_data(:,2);
```

Furthermore, before you ask the program to search for the highest absorbance values in the data, you need to specify which part of the spectrum you want to focus on. For example, the ATR-IR spectrum of antigorite has two absorbance regions: the Si-O absorbance region (650-1250 cm^{-1}) and the O-H absorbance region (3300-3750 cm^{-1}). For the purpose of this example, the program will determine the wavenumber value (t) and intensity (y1) of the highest absorbance peak in the Si-O absorbance region of antigorite. Note that the range 1:1246 denotes the row numbers in the .CSV file, which contain the wavenumber values between 650-1250 cm^{-1}:

```matlab
% Set data range
    t=x(1:1246);
    y1=y(1:1246)';
```

Now that the program knows, which part of the data it needs to analyze, it is possible to perform various operations to analyze the spectral data. For the purposes of our study, we wanted to find the highest absorbance peak in a certain wavenumber range. The 'findpeaks' function in the MATLAB Signal Processing Toolbox can be used to find the absorbance intensity (pks) and wavenumber value (locs) of the highest point in the spectrum.

```matlab
% Peak search
    [pks,locs] = findpeaks(y1,'SortStr','descend','NPeaks',1);
```

The code also specifies that the program should find the single (1) highest absorbance intensity value within the specified range (y1). The input arguments specify that in the output data the peaks should be sorted (SortStr) in descending order from the highest peak to the lowest peak (descend) and that the algorithm should produce the maximum number of positive integer scalar peaks (NPeaks). To export the result of the executed code, you need to define the xpks

and ypks for this iteration. This code tells the program that the wavenumber (xpks) and intensity (ypks) values of the highest absorbance peaks should be exported to the parent folder in .CVS format:

```
% Export data

    xpks=[xpks;t(locs)];

    ypks=[ypks;pks];

    csvwrite([sample,'_pks.csv'],[xpks,ypks]);
```

In order to include all spectra (wavenumber (t) and intensity (y1) values) in first figure, the plot command needs to be included within this iteration:

```
% Figure 1. 2D line plot settings

    plot(t,y1,'-','Color','#191175','LineWidth',1.5);
```

The input arguments ('-', 'Color', '#191175', 'LineWidth', 1.5) specify the visual properties, e.g. the style, color and width, of the spectra and they can be modified to suit the needs of the user. Finally, to terminate this iteration, type in end:

```
end
```

It is now possible to press enter and let the program analyze the data. Data of the wavenumber and intensity values of the highest intensity absorbance peaks can be used to create spectral maps and the data can be analyzed further by using statistical methods or by performing more advanced calculations. Most data processing software also offer useful ways of visualizing the data. In case of MATLAB, it is possible to plot the results of the peak search by entering the following code after the code for Iteration 1:

```
    plot(xpks,ypks,'ko','MarkerFaceColor','w','MarkerSize',8);
```

```
    xlim([650 1250]);

    ylim([0 1.2]);
```

The 2D line plot (Fig. 2) created by the code above contains both the spectral data (t, y1), which was "on hold" and the highest intensity peak data (xpks,ypks). It is possible to modify the axis range (xlim and ylim), labels, style, font etc. by modifying the input arguments (e.g. 'MarkerFaceColor') to make adjustments to the visual output of the figure. The full input arguments that were used to create the figures in this chapter are detailed in Appendix 1. The print command can be used to save the figure. In this example, the 2D line plot was saved as .png file with 300 pixel resolution:

```
    savename=[sample,'_highest_peaks.png'];

    print(savename, '-dpng', '-r300');
```

Spectral plots, such as Figure 2, are a good way to visualize peak distribution data but in the case of larger datasets it is also useful to plot the data in some other ways in order to get a better grip on the overall variation within the dataset. Another figure showing the peak distribution can be created by using the 'figure' and 'plot' commands and adjusting the wavenumber range:

```
figure('Position', [400 700 1000 500]);

plot(xpks,ypks,'o','Color','#191175','MarkerFaceColor','w','MarkerSi
ze',8);

ylim([0 1.2]);

xlim([945 970]);
```

The second figure is a scatter plot, which shows the distribution of absorbance intensities and wavenumber values of the highest intensity absorbance peaks of antigorite within the wavenumber range 945-970 cm^{-1} (Fig. 3). The scatterplot of antigorite Si-O absorbance peaks

highlights the wide wavenumber absorbance range (between 946-969 cm^{-1}) in sample Ts33. It also shows that the data quality of the ATR-IR map is quite good, since most of the measurements have relatively high absorbance intensity values.

Histogram of the wavenumber values of the highest intensity peaks is another useful way of looking for patterns in the data:

```
figure('Position', [400 700 1000 500]);

histogram(xpks,'BinWidth',1,'FaceColor','#191175','EdgeColor','w','FaceAlpha',1)

ylim([0 700]);

xlim([945 970]);
```

The histogram of sample Ts33 (Fig. 4), for example, illustrates that the Si-O absorbance values within the mapping data have a bimodal distribution, with one high frequency region around ~961 cm^{-1} and another around ~954 cm^{-1}.

3.2. Reconstructing spectral maps

Generally, the aim of spectral mapping of mineral microstructures is to represent the processed data as a map so that it can be compared to the microstructures of the sample. Hence, after data processing, the results need reconstructed back to map form. To do this, the grid dimensions of the map need to be extracted from the spectrometer. The grid data should be saved in tabular format (e.g. an Excel table or a CSV file) in the same folder with the parent folder as the previous files. To start reconstructing the spectral map with the processed data, enter the following code in the MATLAB command window:

```
sample='Ts33';

filename_csv='Ts33_pks';

filename_xy='Ts33_XY';
```

```
pks_data=readmatrix([filename_csv,'.csv']);

xy_data=readmatrix([filename_xy,'.csv']);
```

Let the program know that the spectral peak information (pks_data) is in the filename_csv file and that the grid dimension information (xy_data) is in the filename_xy file and use the 'readmatrix' command to tell the program to read the files.

Next, it's time to set the array size and the target variable you want to use to construct the map. In this example, the x and y coordinates are in the 1st and 2nd column of the Ts33_XY.csv file. The z1 and z2 values, which in this example are the intensity and wavenumber values of the antigorite Si-O absorbance peak, are in the 1st and 2nd column of the Ts33_pks.csv file.

```
Array_size=size(pks_data)

x=xy_data(:,1);

y=xy_data(:,2);

z1=pks_data(:,1);

z2=pks_data(:,2);
```

Next, you need to determine the longitude and latitude arrays of the map by using the 'unique' command. This command will pick out each unique value of x and y, which are needed to determine the dimensions of the map.

```
lon = unique(x) ;

lat = unique(y) ;
```

After this, the program needs to know how to put all the data together:

```
peaks=[];intensity=[];
```

```
for n=1:1:length(z1)

    ilon = find(lon==x(n));

    ilat = find(lat==y(n));

        peaks(ilat,ilon) = z1(n);

    intensity(ilat,ilon) = z2(n);

end
```

The data we want to display are the wavenumber values (peaks) and intensities (intensity) of the antigorite Si-O absorbance peaks. The 'find' command returns a vector containing the linear indices of each nonzero element in longitudinal (lon) and latitudinal (lat) arrays. This means that the program will determine how many times the longitudinal and latitudinal arrays, which were determined in the previous step, appear within the x (n) and y (n) datasets. In this example, the longitudinal and latitudinal arrays appear 37 and 73 times, respectively, within the x and y datasets and thus the dimensions of the map are 37x73 pixels. The final step of this operation shown above is to combine the peak intensity and wavenumber information with the dimensional information of the map.

To draw a map with the correct dimensions, the program needs to be informed that the step size used for mapping was 50 µm:

```
xmicron = [lon(1):50:lon(end)];

ymicron = [lat(1):50:lat(end)];
```

Finally, use the 'figure' command to create the map. The pseudocolor or 'pcolor' command lets you display matrix data as an array of colored cells. In this case the matrix dimensions are the values of 'xmicron' and 'ymicron', defined in the previous step. It is necessary to create two separate maps to show both the wavenumber values (5a) and intensities (5b) of the highest intensity Si-O absorbance peaks:

```
figure;

pcolor(xmicron,ymicron,peaks);

axis equal tight;

axis off;

shading flat;

cmin=945;cmax=970;caxis([cmin cmax]);

figure;

pcolor(xmicron,ymicron,intensity);

axis equal tight;

axis off;

shading flat;

cmin=0.5;cmax=1;caxis([cmin cmax]);
```

To show the spectral data properly, the input options 'axis equal tight' and 'axis shading flat' should be chosen. Also, to bring out the differences in the spectral data, you should set minimum (cmin) and maximum (cmax) values for the color scale. In this example, we are interested in looking at variation in the antigorite Si-O absorbance within the wavenumber range of 945-970 cm^{-1} and the absorbance intensity range of 0.5-1. As with the previous figures in this chapter, there are various other input options that can be used to modify the visual style of the maps, which are detailed in Appendix 2. Finally, use the print command to save the figures in the image format of your choice.

```
% save figure

    savename=[sample,'_intensity_map.png'];

    print(savename, '-dpng', '-r300');
```

4. DISCUSSION

The ATR-IR mapping algorithm introduced in this study provides a simple but effective way to process large amounts of spectral data. The 'findpeaks' function that we used to determine the highest intensity absorbance peaks works simply by picking the highest numerical value out of the dataset and thus determining the peaks of thousands of spectra can be done in a matter of minutes. The 'findpeaks' function can be easily applied to study the variation in the wavenumber value of a single absorbance peak. For example, the ATR-IR map containing the wavenumber values of the highest intensity Si-O absorbance peaks in sample Ts33 (Fig. 5a), shows the bimodal distribution of the absorbance peaks between the fibrous antigorite veins ($\sim$961 cm^{-1}) and the matrix ($\sim$954 cm^{-1}). More low intensity ATR-IR absorbance values are recorded from the antigorites in the matrix than from antigorites in the fibrous vein (Fig. 5b). The low intensity measurements are due to surface defects and fine grained magnetite grains within the matrix (Fig. 1), both of which can cause distortions in the ATR-IR spectra of antigorite. ATR-IR measurements are made by lowering the ATR-crystal of the sample surface and running the infrared beam through the ATR-crystal and thus anything that obstructs the direct contact between the ATR-crystal and the target mineral will negatively affect the measurement results. Hence, samples studied using ATR-IR spectroscopy should be carefully polished.

There are also various filtering and fitting functions available that can help process noisy or distorted spectra. Commonly used methods of spectroscopic data processing, such as the spectral peak fitting software PeakFit 4.12., use complicated functions, such as Gaussian response function with Fourier deconvolution/filtering algorithm, to determine the positions of absorbance peaks. Running such complicated functions consumes considerably more time and often each spectrum needs to be processed individually. However, running the data through more advanced algorithms will produce a more reliable result. For example, Rooney et al.

(2018), who compiled Raman maps of serpentine minerals in fault rocks, used the Witec Project Plus software to determine the average hydroxyl group spectra of antigorite, chrysotile and lizardite and then used a basis analysis function to fit reference spectra with the mapping spectra. This type of approach will diminish error caused by spectral distortion of one absorbance peak and one of our goals for future research is to build a more sophisticated ATR-IR data processing algorithm, which includes options for Gaussian and Lorentzian peak fitting functions.

The quantitative processing of spectral data has a wide range of applications far beyond just ATR-IR mapping. A modified version of the algorithm outlined in this chapter has been already applied in analyzing Raman spectra of quartz inclusions in kyanite. This research, under development at Nagoya University, is part of developing a new Raman geothermobarometry method. The method is based on previous research on quartz inclusions in garnet by Kouketsu et al. (2014) and it works by measuring the residual pressure recorded in quartz inclusions by determining the distance of two quartz absorbance peaks and comparing the results to a previously determined standard value. Applying a modified version of the quantitative method outlined in this chapter did not only speed up the data processing, but processed Raman mapping data of quartz inclusions also revealed that the residual pressures recorded from the sides of the quartz inclusion were unreliable and should not be included in the pressure estimation. Indeed, in a field aptly dubbed "Thermoba-Raman-try" by Matthew Kohn (2014), our algorithm could be used to process Raman data of a large amount of different mineral host and inclusion pairs, which can be used to estimate metamorphic pressures and temperatures.

Another spectroscopic method that has been under development at the Research Group of Mineralogy and Petrology at Nagoya University, is the quantitative determination of water content in olivine using Fourier transform infrared spectroscopy (FT-IR). Several workers (Bell

et al., 2003; Matveev and Stachel, 2007; Nakashima et al., 1995) have used Fourier transform infrared spectroscopy (FT-IR) to measure water content in nominally anhydrous minerals, such as quartz and olivine, by measuring the absorbance intensity of the O-H absorbance peak in the mid-infrared range. With slight modifications, the algorithm proposed in this chapter can be applied to study variation in water content in the FT-IR mapping data of various different minerals.

One more complex mineralogical method of relevance, that could benefit from a more quantitative approach, is Raman spectra of carbonaceous materials (RSCM) geothermometry, originally developed by Beyssac et al. (2002). This method has recently become very popular in determining the thermal structure of various types of metamorphic rocks (e.g. Aoya et al., 2010; Kouketsu et al., in print; Negro et al., 2006) but obtaining credible data requires determining the intensity and width of four individual Raman peaks and calculating the ratios of said peaks in tens or hundreds of spectra. Determining the peak positions spectrum by spectrum is laborious and susceptible to human bias and error. Thus, one of the aims of future development for this method is to find a way to include more complex calculations within the algorithm.

5. CONCLUSIONS

The spectral data processing algorithm introduced in this chapter was developed to study attenuated total reflection infrared spectroscopy (ATR-IR) mapping data of serpentinite samples. While the algorithm presented here is quite simple, I believe that it provides a more accurate and efficient way to process large datasets of spectral data and with few modifications this method could be applied more widely in the field of vibrational spectroscopy. Further development of fitting and filtering functions and the addition of more complex spectral

calculation options are necessary to unlock the full range of information embedded in the spectral data of rocks and minerals.
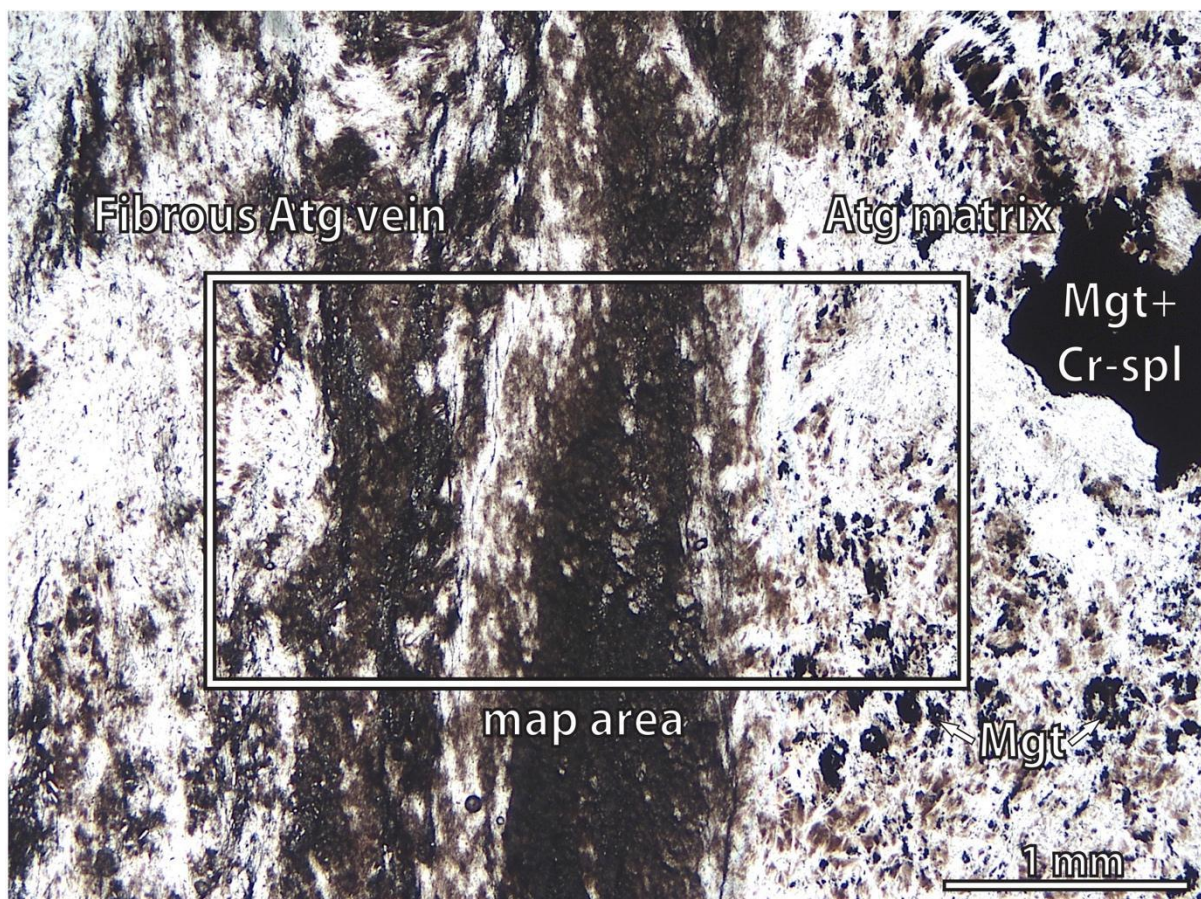
Figure 1. The ATR-IR mapping area in sample Ts33. The ATR-IR map is from the contact zone of a fibrous antigorite (Atg) vein and platy antigorite matrix, which also contains fine grained magnetite (Mgt). In addition, this sample contains relict chromian spinel (Chr-spl), within some of the larger magnetite grains.
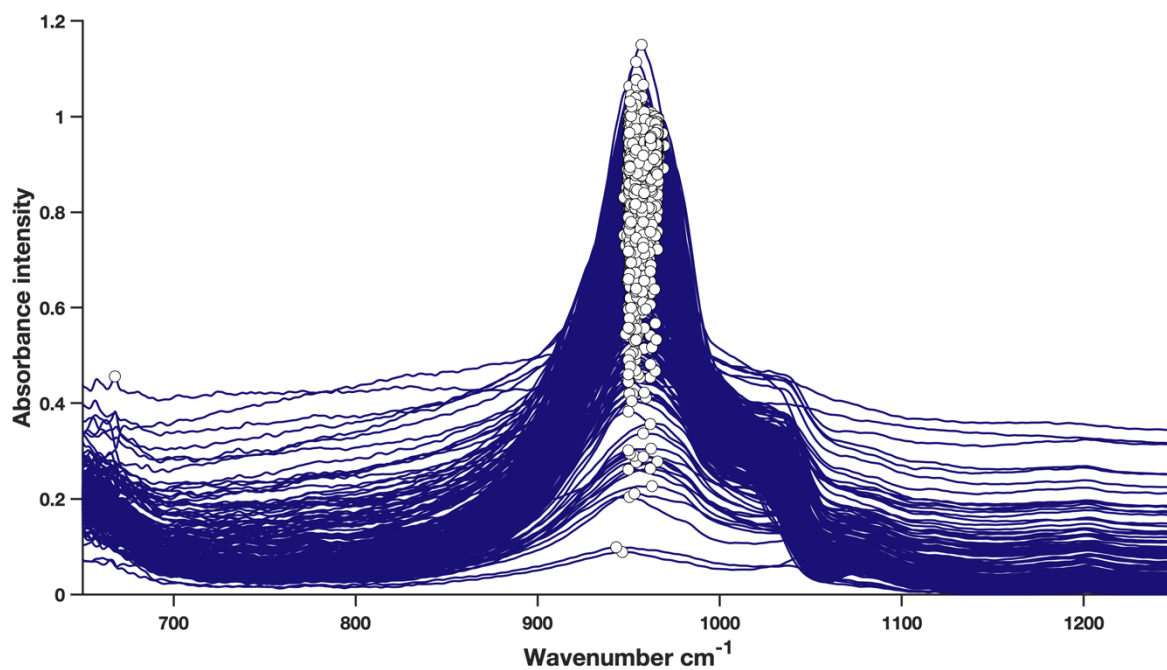
Figure 2. A 2D line plot showing the absorbance intensity and wavenumber value of the highest intensity absorbance peak in the 650-1250 cm^{-1} region of the ATR-IR mapping spectra from sample Ts33. The white dots represent the highest absorbance peaks of each individual measurement.
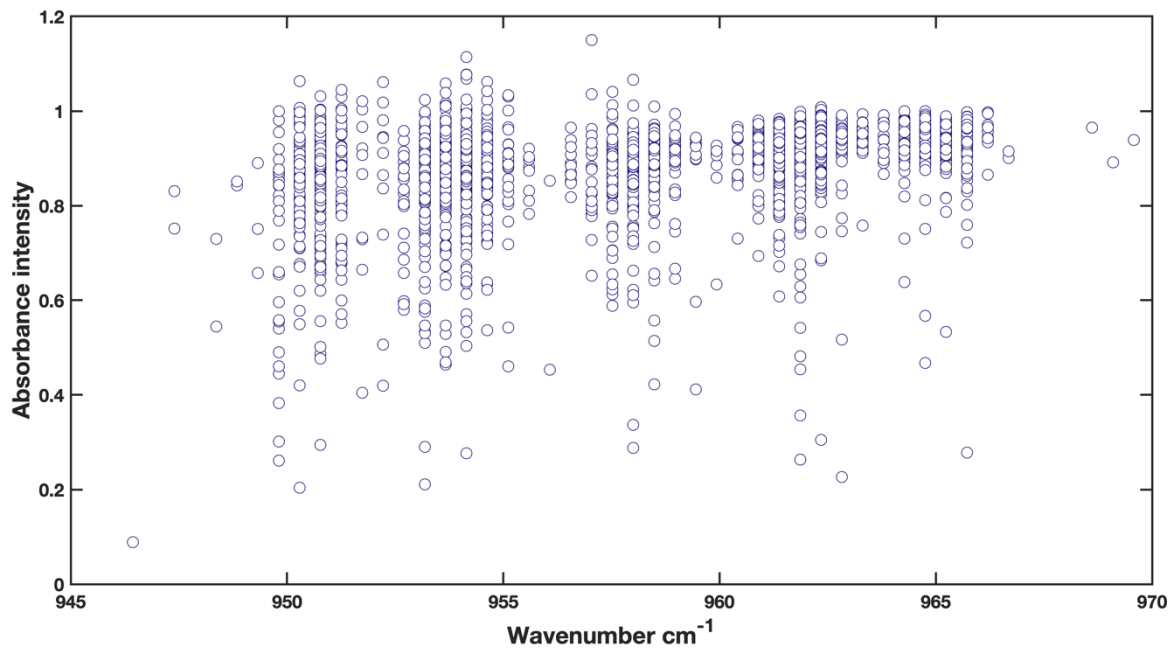
Figure 3. A scatterplot of the absorbance intensity and wavenumber values of highest intensity Si-O absorbance peaks of antigorite in the ATR-IR map of sample Ts33.
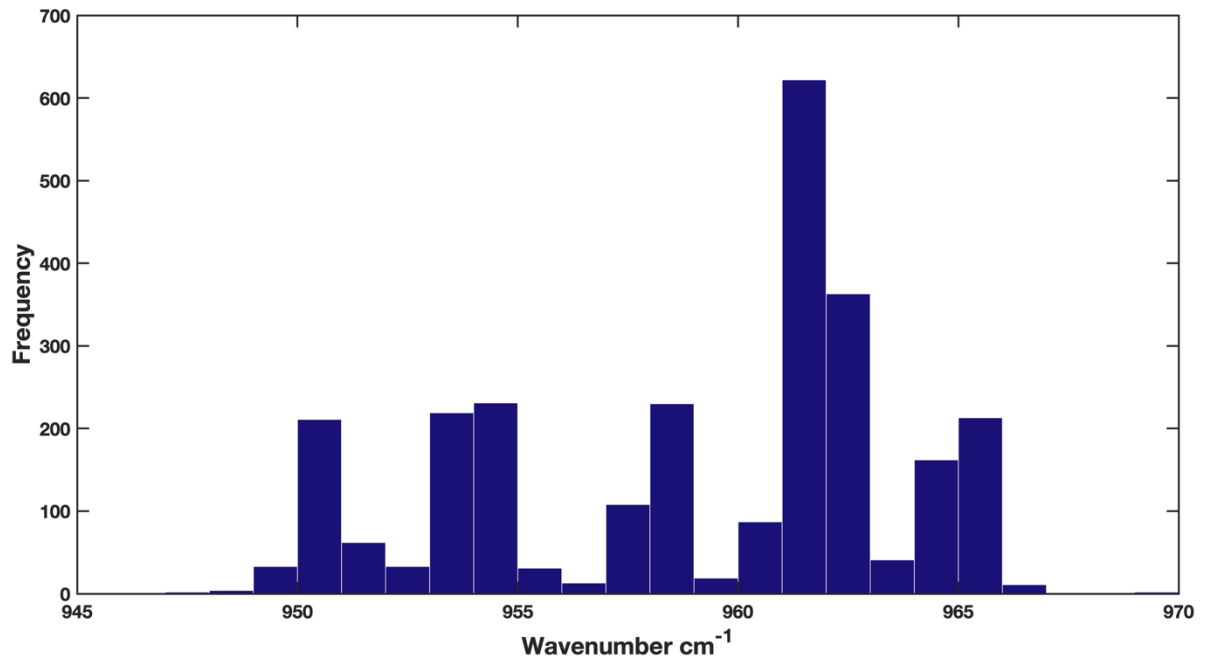
Figure 4. Frequency of highest intensity Si-O absorbance values of antigorite in the ATR-IR map of sample Ts33.

Figure 5. Reconstructed ATR-IR maps of the highest intensity Si-O absorbance peak of antigorites in sample Ts33 showing a) wavenumber values and b) intensities. Step size used for mapping was 50 μm.

ACKNOWLEDGEMENTS

REFERENCES

Alt, J.C., Schwarzenbach, E.M., Früh-Green, G.L., Shanks, W.C., Bernasconi, S.M., Garrido, C.J., Crispini, L., Gaggero, L., Padrón-Navarta, J.A., Marchesi, C., 2013. The role of serpentinites in cycling of carbon and sulfur: Seafloor serpentinization and subduction metamorphism. Lithos, Serpentinites from mid-oceanic ridges to subduction 178, 40–54.

Anbalagan, G., Sivakumar, G., Prabakaran, A.R., Gunasekaran, S., 2010. Spectroscopic characterization of natural chrysotile. Vibrational Spectroscopy 52, 122–127.

Aoya, M., Endo, S., Mizukami, T., Wallis, S.R., 2013. Paleo-mantle wedge preserved in the Sambagawa high-pressure metamorphic belt and the thickness of forearc continental crust. Geology 41, 451–454.

Aoya, M., Kouketsu, Y., Endo, S., Shimizu, H., Mizukami, T., Nakamura, D., Wallis, S., 2010. Extending the applicability of the Raman carbonaceous-material geothermometer using data from contact metamorphic rocks. Journal of Metamorphic Geology 28, 895–914.

Auzende, A.-L., Guillot, S., Devouard, B., Baronnet, A., 2006. Serpentinites in an Alpine convergent setting: Effects of metamorphic grade and deformation on microstructures. European Journal of Mineralogy 18, 21–33.

Bach, W., Klein, F., 2009. The petrology of seafloor rodingites: Insights from geochemical reaction path modeling. Lithos, Recent developments on seafloor petrology and tectonics 112, 103–117.

Bailey, S.W., Banfield, J.F., 1995. Derivation and identification of nonstandard serpentine polytypes. American Mineralogist 80, 1104–1115. https://doi.org/10.2138/am-1995-11-1202

Balan, E., Delattre, S., Roche, D., Segalen, L., Morin, G., Guillaumet, M., Blanchard, M., Lazzeri, M., Brouder, C., Salje, E.K.H., 2011. Line-broadening effects in the powder infrared spectrum of apatite. Phys Chem Minerals 38, 111–122.

Balan, E., Mauri, F., Lemaire, C., Brouder, C., Guyot, F., Saitta, A.M., Devouard, B., 2002a. Multiple Ionic-Plasmon Resonances in Naturally Occurring Multiwall Nanotubes: Infrared Spectra of Chrysotile Asbestos. Physical Review Letters 89.

Balan, E., Saitta, A.M., Mauri, F., Lemaire, C., Guyot, F., 2002b. First-principles calculation of the infrared spectrum of lizardite. American Mineralogist 87, 1286–1290.

Baziotis, I., Tsai, C.-H., Ernst, W.G., Jahn, B.-M., Iizuka, Y., 2017. New P–T constraints on the Tamayen glaucophane-bearing rocks, eastern Taiwan: Perple_X modelling results and geodynamic implications. Journal of Metamorphic Geology 35, 35–54.

Bell, D.R., Rossman, G.R., Maldener, J., Endisch, D., Rauch, F., 2003. Hydroxide in olivine: A quantitative determination of the absolute amount and calibration of the IR spectrum. Journal of Geophysical Research: Solid Earth 108.

Beyssac, O., Goffé, B., Chopin, C., Rouzaud, J.N., 2002. Raman spectra of carbonaceous material in metasediments: a new geothermometer. Journal of Metamorphic Geology 20, 859–871.

Boschi, C., Frueh-Green, G., Escartin, J., 2006. Occurrence and significance of serpentinite-hosted, talc- and AMPHIBOLE-RICH fault rocks in modern oceanic settings and ophiolite complexes: An overview. Ofioliti 31, 129–140.

Bretscher, A., Hermann, J., Pettke, T., 2018. The influence of oceanic oxidation on serpentinite dehydration during subduction. Earth and Planetary Science Letters 499, 173–184.

Brindley, G.W., Wan, H.-M., 1975. Compositions, structures, and thermal behavior of nickel-containing minerals in the lizardite-nepouite series. American Mineralogist 60, 863–871.

Bromiley, G.D., Pawley, A.R., 2003. The stability of antigorite in the systems $MgO\text{-}SiO_2\text{-}H_2O$ (MSH) and $MgO\text{-}Al_2O_3\text{-}SiO_2\text{-}H_2O$ (MASH): The effects of Al^{3+} substitution on high-pressure stability. American Mineralogist 88, 99–108.

Carbonin, S., Martin, S., Tumiati, S., Rossetti, P., 2015. Magnetite from the Cogne serpentinites (Piemonte ophiolite nappe, Italy). Insights into seafloor fluid–rock interaction. European Journal of Mineralogy 27, 31–50.

Chamritski, I., Burns, G., 2005. Infrared- and Raman-Active Phonons of Magnetite, Maghemite, and Hematite: A Computer Simulation and Spectroscopic Study. J. Phys. Chem. B 109, 4965–4968.

Chen, C., Ho, H., Shea, K., Lo, W., Lin, W., Chang, H., Huang, C., Lin, C., Chen, G., Yang, C., 2000. Geological Map of Taiwan. 1: 500,000 scale, Central Geol. Sur., Taiwan.

Chen, Y.-X., Lu, W., He, Y., Schertl, H.-P., Zheng, Y.-F., Xiong, J.-W., Zhou, K., 2019. Tracking Fe mobility and Fe speciation in subduction zone fluids at the slab-mantle interface in a subduction channel: A tale of whiteschist from the Western Alps. Geochimica et Cosmochimica Acta 267, 1–16.

Chih-Ying, Y., 2019. New constraints and interpretations on peak pressure-temperature conditions of metasedimentary rocks in the Yuli belt, eastern Taiwan (Master's thesis). National Dong Hwa University, Hualien, Taiwan.

Debret, B., Andreani, M., Muñoz, M., Bolfan-Casanova, N., Carlut, J., Nicollet, C., Schwartz, S., Trcera, N., 2014. Evolution of Fe redox state in serpentine during subduction. Earth and Planetary Science Letters 400, 206–218.

Debret, B., Bolfan-Casanova, N., Padron-Navarta, J.A., Martin-Hernandez, F., Andreani, M., Garrido, C.J., Sanchez-Vizcaino, V.L., Gómez-Pugnaire, M.T., Munoz, M., Trcera, N., 2015. Redox state of iron during high-pressure serpentinite dehydration. Contributions to Mineralogy and Petrology 169, 36.

Debret, B., Bouilhol, P., Pons, M.L., Williams, H., 2018. Carbonate Transfer during the Onset of Slab Devolatilization: New Insights from Fe and Zn Stable Isotopes. J Petrology 59, 1145–1166.

Debret, B., Millet, M.-A., Pons, M.-L., Bouilhol, P., Inglis, E., Williams, H., 2016. Isotopic evidence for iron mobility during subduction. Geology 44, 215–218.

Deer, W.A., Howie, R.A., Zussman, J., 2009. Rock Forming Minerals: Layered Silicates Excluding Micas and Clay Minerals, Volume 3B. Geological Society of London.

Dewangga, D., 2019. Petrological characterization of serpentinites and related rocks from the Yuli belt, eastern Taiwan (Master's thesis). National Dong Hwa University, Hualien, Taiwan.

Dobson, D.P., Meredith, P. G., Boon, S. A., 2002. Simulation of Subduction Zone Seismicity by Dehydration of Serpentine. Science 298, 1407–1410.

Dódony, I., Buseck, P.R., 2004. Serpentines Close-Up and Intimate: An HRTEM View. International Geology Review 46, 507–527.

Enami, M., 2006. Mineralogical methods for identification of asbestos and their limitations. Japanese Magazine of Mineralogical and Petrological Sciences 35, 11–21.

Enami, M., Wallis, S.R., Banno, Y., 1994. Paragenesis of sodic pyroxene-bearing quartz schists: implications for the PT history of the Sanbagawa belt. Contributions to Mineralogy and Petrology 116, 182–198.

Endo, S., Wallis, S., Hirata, T., Anczkiewicz, R., Platt, J., Thirlwall, M., Asahara, Y., 2009. Age and early metamorphic history of the Sanbagawa belt: Lu–Hf and P–T constraints from the Western Iratsu eclogite. Journal of Metamorphic Geology 27, 371–384.

Evans, B.W., 2004. The Serpentinite Multisystem Revisited: Chrysotile Is Metastable. International Geology Review 46, 479–506.

Evans, B.W., Hattori, K., Baronnet, A., 2013. Serpentinite: What, Why, Where? Elements 9, 99–106.

Farmer, V.C., Mineralogical Society (Great Britain) (Eds.), 1974. The Infrared spectra of minerals, Mineralogical Society monograph. Mineralogical Society, London.

Groppo, C., Rinaudo, C., Cairo, S., Gastaldi, D., Compagnoni, R., 2006. Micro-Raman spectroscopy for a quick and reliable identification of serpentine minerals from ultramafics. European Journal of Mineralogy 18, 319–329.

Hacker, B.R., Peacock, S.M., Abers, G.A., Holloway, S.D., 2003. Subduction factory 2. Are intermediate-depth earthquakes in subducting slabs linked to metamorphic dehydration reactions? Journal of Geophysical Research: Solid Earth 108.

Hattori, K.H., Guillot, S., 2003. Volcanic fronts form as a consequence of serpentinite dehydration in the forearc mantle wedge. Geology 31, 525–528.

Higashino, T., 1990. The higher grade metamorphic zonation of the Sambagawa metamorphic belt in central Shikoku, Japan. Journal of Metamorphic Geology 8, 413–423.

Isozaki, Y., Itaya, T., 1990. Chronology of Sanbagawa metamorphism. Journal of Metamorphic Geology 8, 401–411.

Jung, H., Green II, H.W., Dobrzhinetskaya, L.F., 2004. Intermediate-depth earthquake faulting by dehydration embrittlement with negative volume change. Nature 428, 545–549.

Kato, T., 2005. New Accurate Bence-Albee α-Factors for Oxides and Silicates Calculated from the PAP Correction Procedure. Geostandards and Geoanalytical Research 29, 83–94.

Kawahara, H., Endo, S., Wallis, S.R., Nagaya, T., Mori, H., Asahara, Y., 2016. Brucite as an important phase of the shallow mantle wedge: Evidence from the Shiraga unit of the Sanbagawa subduction zone, SW Japan. Lithos 254–255, 53–66.

Keyser, W., Tsai, C.-H., Iizuka, Y., Oberhänsli, R., Ernst, W.G., 2016. High-pressure metamorphism in the Chinshuichi area, Yuli belt, eastern Taiwan. Tectonophysics, Geodynamics and Environment in East Asia, GEEA 2014 692, 191–202.

Kohn, M.J., 2014. "Thermoba-Raman-try": Calibration of spectroscopic barometers and thermometers for mineral inclusions. Earth and Planetary Science Letters 388, 187–196.

Kouketsu, Y., Ando, K., Sakaguchi, I., Igami, Y., Miyake, A., Kawahara, H., Wallis, S., In review. Serpentinization history recorded in antigorite: A case study of the Shiraga

serpentinites, Sanbagawa metamorphic belt, southwest Japan. Contributions to Mineralogy and Petrology.

Kouketsu, Y., Enami, M., Mizukami, T., 2010. Omphacite-bearing metapelite from the Besshi region, Sambagawa metamorphic belt, Japan: Prograde eclogite facies metamorphism recorded in metasediment. Journal of Mineralogical and Petrological Sciences 105, 9–19.

Kouketsu, Y., Nishiyama, T., Ikeda, T., Enami, M., 2014. Evaluation of residual pressure in an inclusion–host system using negative frequency shift of quartz Raman spectra. American Mineralogist 99,

Kouketsu, Y., Sadamoto, K., Umeda, H., Kawahara, H., Nagaya, T., Taguchi, T., Mori, H., Wallis, S., Masaki, E., In print. Thermal structure in subducted units from continental Moho depths in a paleo subduction zone, the Asemigawa region of the Sanbagawa metamorphic belt, SW Japan. Journal of Metamorphic Geology n/a.

Kouketsu, Y., Tsai, C.-H., Enami, M., 2019. Discovery of unusual metamorphic temperatures in the Yuli belt, eastern Taiwan: New interpretation of data by Raman carbonaceous material geothermometry. Geology 47, 522–526.

Lan, C.H., 2011. Metamorphic petrogenesis and whole- rock geochemistry of tectonic blocks in the Wanjung Area, Eastern Taiwan (Master's Thesis). National Dong Hwa University, Hualien, Taiwan,.

Lin, M.L., 1999. Litho-stratigraphy and structural geology of Wanjung area, eastern Taiwan and their implications. Journal of the Geological Society of China 42, 247–67.

Liou, J.G., 1981. Petrology of metamorphosed oceanic rocks in the Central Range of Taiwan. Memoir of the Geological Society of China 291–341.

Lo, C.-H., Yui, T.-F., 1996. 40Ar/39Ar Dating of High-Pressure Rocks in the Tananao Basement Complex, Taiwan. Journal-Geological Society Of China-Taiwan 39, 13–30.

Lo, Yun-Chieh, Chen, Chih-Tung, Lo, Ching-Hua, Chung, Sun-Lin, Lo, Y.-C, Chen, C.-T, Lo, C.-H, Chung, S.-L, 2020. Ages of ophiolitic rocks along plate suture in Taiwan orogen: Fate of the South China Sea from subduction to collision.

Lowenstern, J.B., Pitcher, B.W., 2013. Analysis of H_2O in silicate glass using attenuated total reflectance (ATR) micro-FTIR spectroscopy. American Mineralogist 98, 1660–1668.

Manning, C.E., 2004. The chemistry of subduction-zone fluids. Earth and Planetary Science Letters 223, 1–16.

Matveev, S., Stachel, T., 2007. FTIR spectroscopy of OH in olivine: A new tool in kimberlite exploration. Geochimica et Cosmochimica Acta 71, 5528–5543.

Mellini, M., Fuchs, Y., Viti, C., Lemaire, C., Linarès, J., 2002. Insights into the antigorite structure from Mössbauer and FTIR spectroscopies. European Journal of Mineralogy 14, 97–104.

Mellini, M., Trommsdorff, V., Compagnoni, R., 1987. Antigorite polysomatism: behaviour during progressive metamorphism. Contributions to Mineralogy and Petrology 97, 147–155.

Merkulova, M., Muñoz, M., Vidal, O., Brunet, F., 2016. Role of iron content on serpentinite dehydration depth in subduction zones: Experiments and thermodynamic modeling. Lithos 264, 441–452.

Milliken, R.E., Mustard, J.F., 2005. Quantifying absolute water content of minerals using near-infrared reflectance spectroscopy. Journal of Geophysical Research: Planets 110.

Moody, J.B., 1976. Serpentinization: a review. Lithos 9, 125–138.

Nakashima, S., Matayoshi, H., Yuko, T., Michibayashi, K., Masuda, T., Kuroki, N., Yamagishi, H., Ito, Y., Nakamura, A., 1995. Infrared microspectroscopy analysis of water distribution in deformed and metamorphosed rocks. Tectonophysics, Influence of Fluids on Deformation Processes in Rocks 245, 263–276.

Negro, F., Beyssac, O., Goffé, B., Saddiqi, O., Bouybaouène, M.L., 2006. Thermal structure of the Alboran Domain in the Rif (northern Morocco) and the Western Betics (southern Spain). Constraints from Raman spectroscopy of carbonaceous material. Journal of Metamorphic Geology 24, 309–327.

O'Hanley, D. S., Dyar, M. D., 1993. The compositionof lizardite 1T and the formation of magnetitein serpentinites. American Mineralogist 78, 391–404.

Okamoto, K., Shinjoe, H., Katayama, I., Terada, K., Sano, Y., Johnson, S., 2004. SHRIMP U–Pb zircon dating of quartz-bearing eclogite from the Sanbagawa Belt, south-west Japan: implications for metamorphic evolution of subducted protolith. Terra Nova 16, 81–89.

Padrón-Navarta, J.A., Hermann, J., Garrido, C.J., Sánchez-Vizcaíno, V.L., Gómez-Pugnaire, M.T., 2010. An experimental investigation of antigorite dehydration in natural silica-enriched serpentinite. Contributions to Mineralogy and Petrology 159, 25.

Padrón-Navarta, J.A., López Sánchez-Vizcaíno, V., Garrido, C.J., Gómez-Pugnaire, M.T., 2011. Metamorphic Record of High-pressure Dehydration of Antigorite Serpentinite to

Chlorite Harzburgite in a Subduction Setting (Cerro del Almirez, Nevado–Filábride Complex, Southern Spain). J Petrology 52, 2047–2078.

Padrón-Navarta, J.A., Sánchez-Vizcaíno, V.L., Garrido, C., Gómez-Pugnaire, M., Jabaloy, A., Capitani, G., Mellini, M., 2008. Highly ordered antigorite from Cerro del Almirez HP–HT serpentinites, SE Spain. Contributions to Mineralogy and Petrology 156, 679.

Padrón-Navarta, J.A., Sánchez-Vizcaíno, V.L., Hermann, J., Connolly, J.A.D., Garrido, C.J., Gómez-Pugnaire, M.T., Marchesi, C., 2013. Tschermak's substitution in antigorite and consequences for phase relations and water liberation in high-grade serpentinites. Lithos, Serpentinites from mid-oceanic ridges to subduction 178, 186–196.

Peacock, S. M., 2001. Are the lower planes of double seismic zones caused by serpentine dehydration in subducting oceanic mantle? Geology 29, 299–302.

Peacock, S.M., 1987. Serpentinization and infiltration metasomatism in the Trinity peridotite, Klamath province, northern California: implications for subduction zones. Contr. Mineral. and Petrol. 95, 55–70.

Peters, D., Bretscher, A., John, T., Scambelluri, M., Pettke, T., 2017. Fluid-mobile elements in serpentinites: Constraints on serpentinisation environments and element cycling in subduction zones. Chemical Geology 466, 654–666.

Post, J.L., Borer, L., 2000. High-resolution infrared spectra, physical properties, and micromorphology of serpentines. Applied Clay Science 16, 73–85.

Rinaudo, C., Gastaldi, D., Belluso, E., 2003. Characterization of Chrysotile, Antigorite and Lizardite by FT-Raman Spectroscopy. The Canadian Mineralogist 41, 883–890.

Rooney, J.S., Tarling, M.S., Smith, S.A.F., Gordon, K.C., 2018. Submicron Raman spectroscopy mapping of serpentinite fault rocks. Journal of Raman Spectroscopy 49, 279–286.

Rüpke, L.H., Morgan, J.P., Hort, M., Connolly, J.A.D., 2004. Serpentine and the subduction zone water cycle. Earth and Planetary Science Letters 223, 17–34.

Sakaguchi, I., Kouketsu, Y., Michibayashi, K., Wallis, S.R., 2020. Attenuated total reflection infrared (ATR–IR) spectroscopy of antigorite, chrysotile, and lizardite. Journal of Mineralogical and Petrological Sciences 115, 303–312.

Sandmann, S., Nagel, T.J., Froitzheim, N., Ustaszewski, K., Münker, C., 2015. Late Miocene to Early Pliocene blueschist from Taiwan and its exhumation via forearc extraction. Terra Nova 27, 285–291.

Scambelluri, M., Cannaò, E., Gilio, M., 2019. The water and fluid-mobile element cycles during serpentinite subduction. A review. European Journal of Mineralogy 31, 405–428.

Scholz, C.H., 2019. The Mechanics of Earthquakes and Faulting. Cambridge University Press.

Serna, C.J., White, J.L., Velde, B.N., 1979. The effect of aluminium on the infra-red spectra of 7 Å trioctahedral minerals 1. Mineralogical Magazine 43, 141–148.

Šontevska, V., Jovanovski, G., Makreski, P., 2007. Minerals from Macedonia. Part XIX. Vibrational spectroscopy as identificational tool for some sheet silicate minerals. Journal of Molecular Structure, Molecular Spectroscopy and Molecular Structure 2006 834–836, 318–327.

Taguchi, T., Enami, M., 2014. Coexistence of jadeite and quartz in garnet of the Sanbagawa metapelite from the Asemi–gawa region, central Shikoku, Japan. Journal of Mineralogical and Petrological Sciences 109, 169–176.

Trommsdorff, V., Sánchez-Vizcaíno, V.L., Gomez-Pugnaire, M.T., Müntener, O., 1998. High pressure breakdown of antigorite to spinifex-textured olivine and orthopyroxene, SE Spain. Contributions to Mineralogy and Petrology 132, 139–148.

Tsai, C.-H., Iizuka, Y., Ernst, W.G., 2013. Diverse mineral compositions, textures, and metamorphic P–T conditions of the glaucophane-bearing rocks in the Tamayen mélange, Yuli belt, eastern Taiwan. Journal of Asian Earth Sciences, HP-UHP Metamorphic Belts in Asia 63, 218–233.

Ulmer, P., Trommsdorff, V., 1995. Serpentine Stability to Mantle Depths and Subduction-Related Magmatism. Science 268, 858–861.

Velde, B., 1980. Ordering in synthetic aluminous serpentines; infrared spectra and cell dimensions. Phys Chem Minerals 6, 209–220.

Viti, C., Mellini, M., 1997. Contrasting chemical compositions in associated lizardite and chrysotile in veins from Elba, Italy. European Journal of Mineralogy 9, 585–596.

Wallis, S., Okudaira, T., 2016. Paired metamorphic belts of SW Japan: the geology of the Sanbagawa and Ryoke metamorphic belts and the Median Tectonic Line. The geology of Japan 101–124.

Wallis, S.R., Anczkiewicz, R., Endo, S., Aoya, M., Platt, J.P., Thirlwall, M., Hirata, T., 2009. Plate movements, ductile deformation and geochronology of the Sanbagawa belt, SW Japan: tectonic significance of 89–88 Ma Lu–Hf eclogite ages. Journal of Metamorphic Geology 27, 93–105.

Whittaker, E.J.W., Muntus, R., 1970. Ionic radii for use in geochemistry. Geochimica et Cosmochimica Acta 34, 945–956.

Whittaker, E.J.W., Wicks, F.J., 1970. Chemical differences among the serpentine "polymorphs": a discussion. American Mineralogist 55, 1025–1047.

Woods, D., Bain, C., 2014. Total internal reflection spectroscopy for studying soft matter. Soft Matter 10, 1071–1096.

Wunder, B., Wirth, R., Gottschalk, M., 2001. Antigorite Pressure and temperature dependence of polysomatism and water content. European Journal of Mineralogy 13, 485–496.

Yui, T.-F., Lo, C.-H., 1989. High-pressure metamorphosed ophiolitic rocks from the Wanjung area, Taiwan. Proc. Geol. Soc. China 32, 47–62.

Yui, T.-F., Usuki, T., Chen, C.-Y., Ishida, A., Sano, Y., Suga, K., Iizuka, Y., Chen, C.-T., 2014. Dating thin zircon rims by NanoSIMS: the Fengtien nephrite (Taiwan) is the youngest jade on Earth. null 56, 1932–1944.

MATLAB script for determining highest intensity absorbance peaks in spectral data

1. Data directory

```
sample='Ts33';

D = dir([sample,'_spectral_data/','data*']);
```

2. Array size and target variables

```
n=size(D,1);

xpks=[],ypks=[]
```

3. Settings for Figure 1

```
figure ('Position', [400 700 1000 500]);

hold on
```

4. Iteration 1

```
for i = 1:n

% Data for analysis

    filename=D(i).name

    IR_data=csvread([sample,'_spectral_data/',filename]);

% Set source for x and y values

    x=IR_data(:,1);

    y=IR_data(:,2);

% Set data range

    t=x(1:1246);

    y1=y(1:1246)';

% Peak search

    [pks,locs] = findpeaks(y1,'SortStr','descend','NPeaks',1);
```

```
% Export data

    xpks=[xpks;t(locs)];

    ypks=[ypks;pks];

    csvwrite([sample,'_pks.csv'],[xpks,ypks]);

% Figure 1. 2D line plot settings

    plot(t,y1,'-','Color','#191175','LineWidth',1.5);

end
```

5. Figure 1. 2D line plot

```
    plot(xpks,ypks,'ko','MarkerFaceColor','w','MarkerSize',8);

    xlim([650 1250]);ylim([0 1.2]);

    xlabel('Wavenumber cm^-^1');ylabel('Absorbance intensity');

    ax=gca;

    ax.LineWidth=1.5;

    ax.FontSize = 13;

    ax.FontWeight='bold';

    ax.LabelFontSizeMultiplier = 1.3;

    ax.TickDir = 'out';

    savename=[sample,'_highest_peaks.png'];

    print(savename, '-dpng', '-r300');
```

6. Figure 2. Scatter plot

```
figure('Position', [400 700 1000 500]);

plot(xpks,ypks,'o','Color','#191175','MarkerFaceColor','w','MarkerSize'
,8);

ylim([0 1.2]);

xlim([945 970]);
```

```
ax=gca;

    ax.LineWidth=1.5;

    ax.FontSize = 13;

    ax.FontWeight='bold';

    ax.LabelFontSizeMultiplier = 1.3;

xlabel('Wavenumber cm^-^1');ylabel('Absorbance intensity');

 % save figure

    savename=[sample,'_scatter_plot.png'];

    print(savename, '-dpng', '-r300');
```

7. Figure 3. Histogram

```
figure('Position', [400 700 1000 500]);

histogram(xpks,'BinWidth',1,'FaceColor','#191175','EdgeColor','w','Face
Alpha',1)

ylim([0 700]);

xlim([945 970]);

xlabel('Wavenumber cm^-^1');ylabel('Frequency');

ax=gca;

    ax.LineWidth=1.3;

    ax.FontSize = 13;

    ax.FontWeight='bold';

    ax.LabelFontSizeMultiplier = 1.3;

 % save figure

    savename=[sample,'_histogram.png'];

    print(savename, '-dpng','-r300');
```

Published with MATLAB® R2019a

APPENDIX 2

MATLAB script for reconstructing spectral maps

1. Data directory

```
sample='Ts33';

filename_csv='Ts33_pks';

filename_xy='Ts33_XY';

pks_data=readmatrix([filename_csv,'.csv']);

xy_data=readmatrix([filename_xy,'.csv']);
```

2. Array size and target variables

```
Array_size=size(pks_data)

x=xy_data(:,1);

y=xy_data(:,2);

z1=pks_data(:,1);

z2=pks_data(:,2);
```

3. Get longitude and latitude arrays

```
lon = unique(x) ;

lat = unique(y) ;
```

4. Define the dimensions of the map

```
peaks=[];intensity=[];

for n=1:1:length(z1)

    ilon = find(lon==x(n));
```

```
    ilat = find(lat==y(n));

        peaks(ilat,ilon) = z1(n);

    intensity(ilat,ilon) = z2(n);

end
```

5. Prepare to draw an image

```
xmicron = [lon(1):50:lon(end)];

ymicron = [lat(1):50:lat(end)];
```

6. Create an absorbance wavenumber map

```
figure;

pcolor(xmicron,ymicron,peaks);

axis equal tight;

axis off;

shading flat;

cmin=945;cmax=970;caxis([cmin cmax]);

ax=gca;

colormap(jet);

colorbar

c2 = colorbar;

c2.Label.String = 'Wavenumber cm^-^1';

c2.FontSize=11;

c2.FontWeight='bold';

% save figure
```

```matlab
    savename=[sample,'_absorbance_map.png'];

    print(savename, '-dpng', '-r300');
```

7. Create an absorbance intensity map

```matlab
figure;

pcolor(xmicron,ymicron,intensity);

axis equal tight;

axis off;

shading flat;

cmin=0.5;cmax=1;caxis([cmin cmax]);

ax=gca;

colormap(jet);

colorbar

c2 = colorbar;

c2.Label.String = 'Absorbance intensity';

c2.FontSize=11;

c2.FontWeight='bold';

% save figure

    savename=[sample,'_intensity_map.png'];

    print(savename, '-dpng', '-r300');
```

Published with MATLAB® R2019a

89